SERIES IN OPTICS AND OPTOELECTRONICS

Advanced Biophotonics

Tissue Optical Sectioning

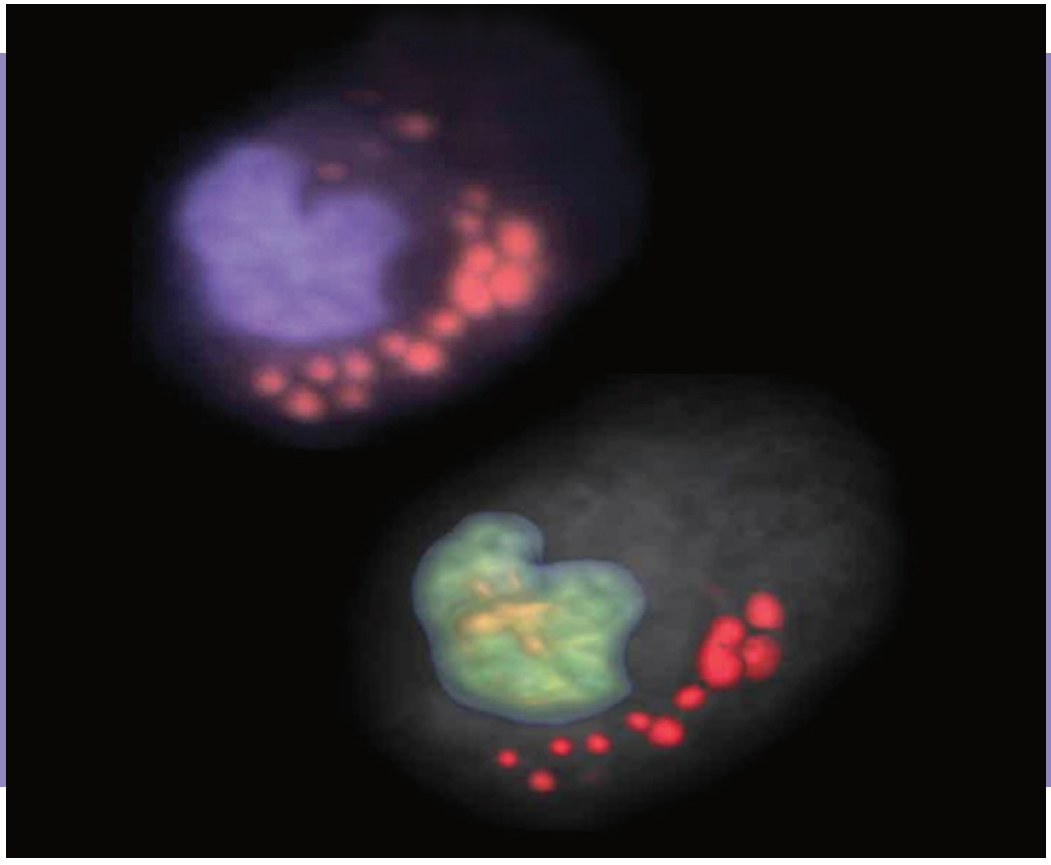

Edited by
Ruikang K. Wang • Valery V. Tuchin

CRC Press
Taylor & Francis Group
A TAYLOR & FRANCIS BOOK

Advanced Biophotonics

SERIES IN OPTICS AND OPTOELECTRONICS

Recent titles in the series

Advanced Biophotonics: Tissue Optical Sectioning
Ruikang K Wang and Valery V Tuchin (Eds.)

Handbook of Silicon Photonics
Laurent Vivien and Lorenzo Pavesi (Eds.)

Microlenses: Properties, Fabrication and Liquid Lenses
Hongrui Jiang and Xuefeng Zeng

Laser-Based Measurements for Time and Frequency Domain Applications: A Handbook
Pasquale Maddaloni, Marco Bellini, and Paolo De Natale

Handbook of 3D Machine Vision: Optical Metrology and Imaging
Song Zhang (Ed.)

Handbook of Optical Dimensional Metrology
Kevin Harding (Ed.)

Biomimetics in Photonics
Olaf Karthaus (Ed.)

Optical Properties of Photonic Structures: Interplay of Order and Disorder
Mikhail F Limonov and Richard De La Rue (Eds.)

Nitride Phosphors and Solid-State Lighting
Rong-Jun Xie, Yuan Qiang Li, Naoto Hirosaki, and Hajime Yamamoto

Molded Optics: Design and Manufacture
Michael Schaub, Jim Schwiegerling, Eric Fest, R Hamilton Shepard, and Alan Symmons

An Introduction to Quantum Optics: Photon and Biphoton Physics
Yanhua Shih

Principles of Adaptive Optics, Third Edition
Robert Tyson

Optical Tweezers: Methods and Applications
Miles J Padgett, Justin Molloy, and David McGloin (Eds.)

Thin-Film Optical Filters, Fourth Edition
H Angus Macleod

Laser Induced Damage of Optical Materials
R M Wood

Advanced Biophotonics

Tissue Optical Sectioning

Edited by
Ruikang K. Wang
Valery V. Tuchin

CRC Press
Taylor & Francis Group
Boca Raton London New York

CRC Press is an imprint of the
Taylor & Francis Group, an **informa** business
A TAYLOR & FRANCIS BOOK

Taylor & Francis
Taylor & Francis Group
6000 Broken Sound Parkway NW, Suite 300
Boca Raton, FL 33487-2742

Version Date: 20130613

International Standard Book Number-13: 978-1-4398-9582-5 (eBook - PDF)

Contents

Preface

Photonics is the science and technology of generation, manipulation, and detection of light. The field uses the quantum-like particles of light, i.e., the photons, instead of electrons to transmit, process, and store information. Biophotonics is recently emerged from the applications of photonics in the fields of biology and medicine. The invention of lasers in the 1960s revolutionized photonics, and made rapid technological advancements that produced useful tools, such as bar code scanners, CD players and laser pointers that are already playing an important part in our daily life. The fluorescence microscope is the first taste of the power of biophotonics that brought us the important molecular information within cells in almost all biological laboratories. Today, biophotonics is widely regarded as the key science upon which the next generation of clinical tools and biomedical research instrumentation will be based. Although nature has used the principle of biophotonics to harness light for photosynthesis, it wasn't until about 10 years ago that a substantial translation of photonics technologies to biological applications began to transform medical and life sciences.

The knowledge of biophotonics essentially includes the fundamentals of many interdisciplinary fields and how they are uniquely related to each other. Researchers and students who are interested in biophotonics should have a solid understanding of the physics of light, and the engineering of devices and instruments that are used to generate, modify, and manipulate light. On the other hand, they must also understand the fundamentals of biology and medicine, such as the molecular and cellular processes that occur in living systems to properly and meaningfully utilize the biophotonics techniques to address their biological questions. Healthy and diseased tissues have differing biological processes in different states; thus, it is also important to have a fundamental understanding of pathophysiology, and common disease states such as cancer, cardiovascular disease, neurodegenerative disease, and infectious disease, to name just a few.

Although still "young," biophotonics is now steadily becoming an important discipline that investigates fundamental principles and develops new optical technology for the interaction of light or photons with biological organisms, tissues, cells, and molecules. One of the most important elements in this discipline is the rapid developments of innovative bio-imaging technologies that brought us the opportunities to visualize tissue organization, biochemical compositions, and functional information about tissue without any harm to its native state. The light with wavelengths between visible and near-infrared ranges is highly scattered within a turbid medium, such as biological tissue. Therefore, the bio-imaging methods that attempt to form images from light passing through tissue can be classified into two categories—ballistic (minimally scattered) optical microscopy and diffuse (multiply scattered) optical tomography. The former provides fine resolution but with a shallow imaging depth in tissue—up to about 1–2 mm, as defined by the optical diffusion limit. The representative technologies in this category include confocal microscopy, multiphoton microscopy, optical coherence tomography, and others.

When incident photons reach their diffusion limit, most of them have undergone tens of scattering events, making the ability to focus the light extremely difficult. Fortunately, diffuse optical tomography can effectively utilize the multiply scattering photons to provide an image that represents information centimeters into tissue, albeit with poor spatial resolution—roughly about one-third of the imaging depth. However, randomized paths of the diffuse photons render the image reconstruction mathematically ill-posed. It still remains a challenge for pure optical imaging to attain fine spatial resolution at depths beyond the optical diffusion limit. Until recently, photoacous-

tic imaging has been developed to break this limitation, in which the researchers innovatively use photon-absorption in tissue that can be converted into ultrasonic waves, which are scattered much less. For this, we have seen impressive progress over just the last few years that has manifested the power of photoacoustic imaging to investigate the molecular and cellular processes that occur in living systems.

Currently, there are a number of professional books (including edited) that were published by different publishers, which describe methods and techniques of biophotonics imaging for medical diagnostics and therapy. Many of them are devoted to specific topics of biomedical optics such as tissue optics, confocal, nonlinear microscopy (including multiphoton microscopy), optical coherence tomography, and others. There is still a lack of a comprehensive imaging book that describes advanced biophotonics imaging methods and techniques intensively developed in recent years, a gap that this current book tries to address. We believe that this assembled book is the next step in presenting contemporary advances in biophotonics imaging and will allow researchers, bioengineers, and medical doctors to be acquainted with major recent bioimaging technologies that apply biophotonics science and technology, which are dispersed in numerous journals of physical, chemical, biophysical, and biomedical profiles.

It is, however, impossible to present all imaging techniques that use the photonics science and technology to address biological and medical questions, particularly when this field is still rapidly evolving and novel imaging methods are constantly conceptualized. The editors hope that this book will be useful for researchers, practitioners, and professionals in the field of biophotonics, and can be used by scientists or professionals in other disciplines, such as laser physics and technology, fiber optics, spectroscopy, materials science, biology, and medicine. Graduate and also undergraduate students specializing in biomedical physics and engineering, biomedical optics and biophotonics will also find this book a useful resource.

This book represents a valuable contribution by well-known experts in the field of biomedical optics and biophotonics with their particular interest in a variety of "hot" biophotonics problems. We greatly appreciate the cooperation and contributions of all authors in the book, who have done great work in the preparation of their chapters.

We would like to thank all those authors and publishers who freely granted permissions to reproduce their copyrighted works. We are grateful to Dr. John Navas, Senior Editor, Physics, of Taylor & Francis/CRC Press, for his idea to publish such a book, valuable suggestions, and help on preparation of the manuscript. We are also very much thankful to Professor Vladimir L. Derbov, Saratov State University, for preparation of the camera-ready manuscript and help in the technical editing of the book.

Ruikang K. Wang

Valery V. Tuchin

The Editors

Ruikang K. Wang, PhD, is Professor of Bioengineering with the University of Washington, Seattle. After two years postdoctoral research training at Glasgow, Scotland, he joined as a Lecturer, and then, Senior Lecturer in Bioimaging Science with Keele Medical School, England. In 2002, he became a chair professor in Biomedical Optics at Cranfield University, England, where he created and directed the Biophotonics and Imaging Laboratory. In 2005, he joined Oregon Health and Science University, Oregon, where he was Professor of Biomedical Engineering and the Director of the Biophotonics and Imaging Laboratory. He is author and co-author of more than 200 peer-reviewed journal articles, one monograph in optical information processing, as well as 12 book chapters. He is a fellow of the Optical Society of America and a fellow of the International Society for Optics and Photonics (SPIE). His current research interests include biophotonics and imaging, optical coherence tomography, optical microangiography, and their applications in neurology, ophthalmology, dermatology and cancer.

Valery V. Tuchin, PhD, holds the Optics and Biophotonics Chair and is a Director of Research-Educational Institute of Optics and Biophotonics at Saratov State University, Head of Laboratory on Laser Diagnostics of Technical and Living Systems, Inst. of Precise Mechanics and Control, RAS, and FiDiPro Professor (Finland Distinguished Professor) of Optoelectronics and Measurement Techniques Laboratory, University of Oulu, Finland. His research interests include biophotonics, biomedical optics and laser medicine, physics of optical and laser measurements. He has authored more than 300 peer-reviewed papers and books, including his latest, *Tissue Optics: Light Scattering Methods and Instrumentation for Medical Diagnosis* (PM166, SPIE Press, second edition, 2007), *Dictionary of Biomedical Optics and Biophotonics* (PM217, SPIE Press, Bellingham, WA, 2012), and three volume *Handbook of Biophotonics* (Wiley-VCH Verlag GmbH & Co. KGaA, Weinheim, 2011-2012. Eds.: J. Popp, V.V. Tuchin, A. Chiou, and S.H. Heinemann). He has been awarded Honored Science Worker of the Russian Federation and SPIE Fellow, and is a Vice-President of the Russian Photobiology Society. In 2007 he was awarded the SPIE Educator Award.

List of Contributors

Jennifer Kehlet Barton
Department of Biomedical Engineering, The University of Arizona, Tucson, Arizona

Chao-Wei Chen
Department of Electrical and Computer Engineering, University of Maryland, College Park, Maryland

Yu Chen
Fischell Department of Bioengineering, University of Maryland, College Park, Maryland

Kenny F. Chou
Department of Bioengineering and Human Photonics Lab, University of Washington, Seattle, Washington

Riccardo Cicchi
National Institute of Optics - National Research Council (INO-CNR), Florence, Italy; European Laboratory for Non-Linear Spectroscopy (LENS), University of Florence, Sesto Fiorentino, Italy

Ryan L. Coe
Department of Bioengineering and Human Photonics Lab, University of Washington, Seattle, Washington

David J. Cuccia
Modulated Imaging Inc., Irvine, California

Andrea Curatolo
Optical+Biomedical Engineering Laboratory (OBEL), School of Electrical, Electronic and Computer Engineering, The University of Western Australia, Crawley, Western Australia, Australia

Susan M. Daly
Department of Physics & Energy, University of Limerick, Ireland

Alexander Doronin
The Jack Dodd Centre for Quantum Technology, Department of Physics, University of Otago, New Zealand

Jacque Duncan
Department of Ophthalmology, University of California, San Francisco, California

Anthony J. Durkin
Beckman Laser Institute and Medical Clinic, University of California, Irvine, California

Nirmalya Ghosh
Department of Physical Sciences, Indian Institute of Science Education and Research (IISER), Kolkata, Mohanpur, West Bengal, India

Christopher A. Girkin
Department of Ophthalmology, University of Alabama at Birmingham, Birmingham, Alabama

Zijian Guo
Optical Imaging Laboratory, Department of Biomedical Engineering, Washington University in St. Louis, St. Louis, Missouri

Timothy R. Hillman
Former address: Optical+Biomedical Engineering Laboratory (OBEL), School of Electrical, Electronic and Computer Engineering, The University of Western Australia, Crawley, Western Australia, Australia

Shuliang Jiao
Department of Ophthalmology, University of Southern California, Los Angeles, California

Brendan F. Kennedy
Optical+Biomedical Engineering Laboratory (OBEL), School of Electrical, Electronic and Computer Engineering, The University of Western Australia, Crawley, Western Australia, Australia

David Layden
Department of Physics and Astronomy, University of Waterloo, Waterloo, Ontario, Canada

Martin J. Leahy
Tissue Optics and Microcirculation Imaging Group, School of Physics, National University of Ireland, Galway, Ireland

Qingming Luo
Britton Chance Center for Biomedical Photonics, Wuhan National Laboratory for Optoelectronics, Huazhong University of Science and Technology, Wuhan, China; Key Laboratory of Biomedical Photonics of Ministry of Education, Huazhong University of Science and Technology, Wuhan, China

Amaan Mazhar
Beckman Laser Institute and Medical Clinic, University of California, Irvine, California

Igor Meglinski
The Jack Dodd Centre for Quantum Technology, Department of Physics, University of Otago, New Zealand

Michael G. Meyer
VisionGate Inc., Phoenix, Arizona

Qin Miao
Department of Bioengineering and Human Photonics Lab, University of Washington, Seattle, Washington

Vasilis Ntziachristos
Institute for Biological and Medical Imaging and Chair for Biological Imaging, Helmholtz Zentrum München and Technische Universität München Ingolstädter Neuherberg, Germany

Francesco S. Pavone
European Laboratory for Non-Linear Spectroscopy (LENS), University of Florence, Sesto Fiorentino, Italy; Department of Physics, University of Florence, Sesto Fiorentino, Italy

Austin Roorda
School of Optometry, University of California, Berkeley, California

Leonardo Sacconi
National Institute of Optics - National Research Council (INO-CNR), Florence, Italy; European Laboratory for Non-Linear Spectroscopy (LENS), University of Florence, Sesto Fiorentino, Italy

David D. Sampson
Optical+Biomedical Engineering Laboratory (OBEL), School of Electrical, Electronic and Computer Engineering, The University of Western Australia, Crawley, Western Australia, Australia

Eric J. Seibel
Department of Mechanical Engineering and Human Photonics Lab, University of Washington, Seattle, Washington

Liang Song
Institute of Biomedical and Health Engineering, Shenzhen Institutes of Advanced Technology, Chinese Academy of Sciences, Shenzhen, China

Hrebesh M. Subhash
Division of Biomedical Engineering, School of Medicine, Oregon Health and Science University, Portland, Oregon

Adrian Taruttis
Institute for Biological and Medical Imaging and Chair for Biological Imaging, Helmholtz Zentrum München and Technische Universität München Ingolstädter Landstr. 1, Neuherberg, Germany

Bruce J. Tromberg
Beckman Laser Institute and Medical Clinic, University of California, Irvine, California

Valery V. Tuchin
Saratov State University, Russian Federation; Institute of Precise Mechanics and Control of RAS, Saratov, Russian Federation; University of Oulu, Finland

Alex Vitkin
Division of Biophysics and Bioimaging, Ontario Cancer Institute; Department of Medical Biophysics and Radiation Oncology, University of Toronto, Toronto, Ontario, Canada

Lihong V. Wang
Optical Imaging Laboratory, Department of Biomedical Engineering, Washington University in St. Louis, St. Louis, Missouri

Ruikang K. Wang
Biophotonics and Imaging Laboratory, Department of Bioengineering, University of Washington, Seattle, Washington

Xin-Cheng Yao
Department of Biomedical Engineering, Vision Sciences Research Center, University of Alabama at Birmingham, Birmingham, Alabama

Hao F. Zhang
Department of Biomedical Engineering, Northwestern University, Evanston, Illinois

Yuhua Zhang
Department of Ophthalmology, University of Alabama at Birmingham, Birmingham, Alabama

Dan Zhu
Britton Chance Center for Biomedical Photonics, Wuhan National Laboratory for Optoelectronics, Huazhong University of Science and Technology, Wuhan, China; Key Laboratory of Biomedical Photonics of Ministry of Education, Huazhong University of Science and Technology, Wuhan, China

1

Monte Carlo Modeling of Photon Migration for the Needs of Biomedical Optics and Biophotonics

Igor Meglinski and Alexander Doronin

The Jack Dodd Centre for Quantum Technology, Department of Physics, University of Otago, New Zealand

Key words: optical diagnostics, Monte Carlo simulation, biotissue imaging

1.1 Introduction

Nowadays optical diagnostics (OD) and photonics-based imaging techniques strongly influence a number of fields including biomedicine, environmental, automotive, combustion, material and life science, etc. [1–3]. OD as well as x-ray, computer tomography, ultrasound imaging, and magnetic resonance are the examples of technologies that have emerged from physics and engineering and have had a significant impact on medical diagnostics and clinical practice [4, 5]. OD encompasses a range of modalities, all of which rely on detecting and analyzing the changes of laser/optical radiation due to interaction with the matter/biological tissues. OD systems and experimental photonics technologies have been significantly improved with the new developments in fiber optics, laser delivery/detection systems [6], Charge Coupled Device (CCD), and therefore become available for various medical and biological applications [2, 5, 7]. Thus, nowadays a number of new OD technologies successfully contribute to healthcare in many medical specialties: dermatology, ophthalmology, oncology, gynecology, gastroenterology, neonatology, etc. [2, 8].

Modern research trends are focused on making medical diagnostics cheaper, faster and consequently more productive by applying new optical techniques incorporated with fast computer algorithms to process and analyze the data in real time. Conceptual design, further optimization and/or modification of the particular experimental OD systems requires careful selection of multiple technical parameters, including intensity, laser beam profile, coherence, polarization, wavelength of incident laser/optical radiation; size, position, numerical aperture, sensitivity of the detector. An

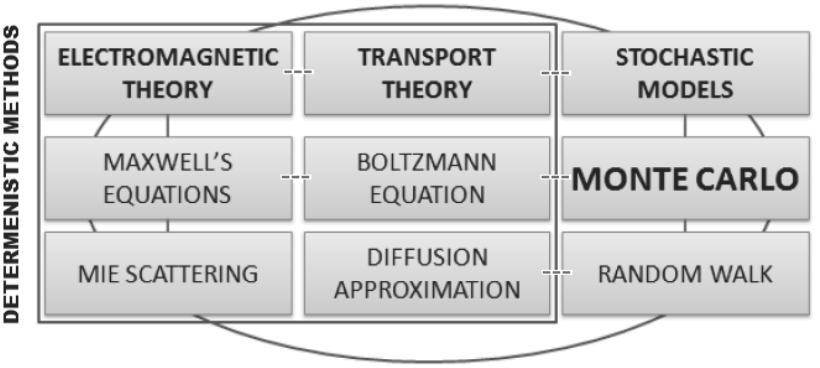

Figure 1.1: Schematic presentation of the major models used to describe optical radiation transfer in turbid media [9–22]. Dashed lines show the relations between different approaches.

estimation of how the spatial and temporal structural alterations in biological tissues can be distinguished by variations of these parameters is also required.

Various aspects of optical radiation propagation within highly scattering randomly inhomogeneous media have been extensively covered in numerous modeling and theoretical studies. These models are tightly related to the structure of the medium and can be separated into two basic categories: stochastic computational and deterministic models (Fig. 1.1).

In **Electromagnetic Theory** propagation of electromagnetic waves through a spatially varying medium, such as tissue, are described by Maxwell's equations [14, 23, 24]. Maxwell's equations are part of fundamental laws of physics and rigorously treat the radiation transfer or transfer of energy of electromagnetic waves.

The description of multiple scattering of optical radiation in the framework of electromagnetic theory employs continuous and discrete models of tissue (Fig. 1.2). In the continuous model, tissue is considered as a random medium whose permittivity $\varepsilon(\mathbf{r},t)$ fluctuates randomly as $\varepsilon_2(\mathbf{r},t)$ with the position about a mean value ε_1, i.e. $\varepsilon(\mathbf{r},t) = \varepsilon_1 + \varepsilon_2(\mathbf{r},t)$. Continuous model combined with electromagnetic theory based on Maxwell's equations could be very effective to study light propagation in biological tissue. However, due to the complex and highly disordered structure of tissues, the defining $\varepsilon(\mathbf{r},t)$ becomes extremely complicated. There have been a number of non-successful attempts to apply this model in the field of tissue optics, except a possibility of determination of refractive indices of various tissues [25]. Therefore, the relevance of electromagnetic theory within tissue optics lies mainly in the study of influence of morphological features of tissue components on distribution of scattered light.

Another modeling approach is based on presenting tissues as an ensemble of discrete scattering and absorbing particles (see Fig. 1.2 b). In this approach, each local center of scattering and absorption corresponds to a statistical average over physically small volume that is a statistical average over several acts of scattering and absorption in cell micro-structure. This theoretical model is well suited for description of light propagation in suspensions of scattering particles (e.g., microspheres). The spatial distribution of light is then obtained by adding the fields, by employing an idea of field perturbation, as a first approximation to the unperturbed single scattering theory [14]. This approach, however, does not lead to solvable equations for practical problems.

Mie computations are mainly realistically performed in order to compute the scattering properties of calibration suspensions of latex spheres [26] and tissue phantoms [26, 27], rather than defining the scattering properties of tissues. Mie theory has serious limitations when applied to describe multiple light scattering by a group of cells in tissue. Perhaps scattering of light in diluted blood samples is

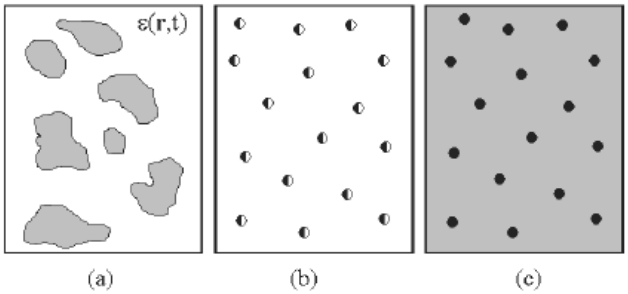

Figure 1.2: Schematic presentation of different tissue models of biological tissues: (a) with random spatial and/or temporal fluctuations of refractive index, (b) an ensemble of randomly distributed scattering and absorbing centers and (c) an ensemble of scattering centers in an absorbing continuum.

one of the few exceptions [2, 28]. Alternative techniques used for simulation of scattering of light on a single particle, e.g., red blood cell [2] are the T-matrix or the extended boundary method based on expansion into spherical harmonics with various boundary conditions, i.e. expressed in terms of integrals over the particle surface of electric and magnetic currents, the method of moments, WKB (Wentzel, Kramers, Brillouin) [14] and RGD approximations.

Radiative transfer is a model describing photon transport in a random scattering medium. The uses of transport theory span across a number of disciplines, including atmospheric and ocean radiative transfer, astrophysics, geophysics and others. The central equation, the radiative transfer equation (RTE) (1.1), mathematically expresses a macroscopic energy balance and describes the statistical average transport of photons and their energy through the turbid medium [14, 29].

$$\underbrace{\left[\underbrace{\frac{1}{v}\frac{\partial}{\partial t}}_{1}+\underbrace{\mathbf{s}\cdot\nabla}_{2}+\underbrace{(\mu_s+\mu_a)}_{3}\right]}L(\mathbf{r},\mathbf{s},t)=\underbrace{\mu_s\oint_{4\pi}p(\mathbf{s},\mathbf{s}')L(\mathbf{r},\mathbf{s}',t)\,d\Omega'}_{4}+\underbrace{Q(\mathbf{r},\mathbf{s},t)}_{5}, \qquad (1.1)$$

where $L(\mathbf{r},\mathbf{s},t)$ is the radiance (the average power flux density at point $\mathbf{r}$ in the direction $\mathbf{s}$ within a unit solid angle at time t), μ_s and μ_a are the optical scattering and absorption coefficients, $p(\mathbf{s},\mathbf{s}')$ is the scattering phase function, $Q(\mathbf{r},\mathbf{s},t)$ is the radiant source function, and v is the speed of light propagation in the medium.

RTE is the equivalent to the equation of Boltzmann's kinetic theory of gases and to the equation of neutron transport theory [30]. The theory is heuristically derived by considering the energy balance of incoming, outgoing, absorbed, scattered, and emitted light of an infinitesimal volume element. It deals with the description of intensity propagation through a scattering medium. The medium is assumed to be homogeneous with constant characteristics of scattering and absorption and containing discrete, bounded regions of absorption and scattering inhomogeneities (see Fig. 1.2 b). Light propagation is envisioned as a stream of photons. A fundamental peculiarity of radiative transfer theory is that intensity of light is only considered, and the method simply ignores the wave phenomena. To enable the correlation between the radiometric, measurable quantities provided by the transport theory and the field characteristics given by electromagnetic theory, it has been proved that RTE can be regarded as an approximate reformulation of Maxwell's equations for a random medium under certain premises [14, 31].

The left-hand and the right-hand sides of (1.1) accounts for photon leaving and entering a small volume element of a medium. In order of appearance, the first term describes the time variation

in a number of photons in the volume, the second term gives the loss of photons in the direction **s**, escaping the observed volume through its boundary surfaces, the third term accounts for photon absorption and scattering out of initial direction **s**. The forth term defines photons gained by scattering process from any directions $\mathbf{s}'$ into the direction **s**. $Q(\mathbf{r},\mathbf{s},t)$ is a number of photons produced by an external light source. This concludes macroscopic energy conservation for a small medium volume. There is a growing interest in validity of RTE for light propagation in biological media and comprehensive reviews of the mathematical solution of RTE are given elsewhere [30, 32, 33].

Integro-differential equations with analytical solutions are often solved numerically by conversion to a system of a linear algebraic equations suitable for numerical solution [2, 14, 34]. The accuracy of the solution depends on the actual number of discretization terms considered. To do this, the radiance $L(\mathbf{r},\mathbf{s})$ (time-dependence is omitted here for brevity) is represented only by its value at discrete values of independent variables. The integration and differentiation operators are replaced by their discrete counterparts, differences and summation. For example, to approximate the angular distribution of the specific intensity, the direction variable is discretized at N values in the RTE. The set of directions is determined by the selected quadrature method. Historically this was not rigorously derived from the transport equation, but was derived using heuristic arguments. Two-flux, or so-called Kubelka-Munk theory [35, 36], and four-flux theories have been used extensively for this purpose. The two-flux theory relates the propagation of opposing light fluxes to scattering and absorption coefficients of a medium. The two-flux model is inadequate for describing a collimated beam incident to a tissue surface. In this case, the four-flux model is utilized, where the fluxes separate into collimated flux (forward and backward) and a diffuse flux (forward and backward). A further refinement of the four-flux theory can be obtained by considering fluxes in more directions. To take into account the effect of finite collimated beam, two more radial fluxes are added, one directed inwards and the other outwards from the main axes of the collimated beam. An example of using the discrete ordinate method for imaging reconstruction in optical diffuse tomography is given in [37].

Alternatively, the discretization can be performed in terms of N small solid angles (cones) qualified by cosine of angles between the initial direction of photon packets and direction of scattering, $\mu_i = \cos(\mathbf{s}\cdot\mathbf{s}')$. The phase function is then substituted by a redistribution matrix with elements, $h(\mu_i,\mu_j)$, corresponding to the fraction of incident light in a cone μ_i, which is scattered into a cone μ_j.

The adding-doubling method is based on this discretization for a slab of tissue, thin along the z-axis and of infinite extent in the xy-plane [38]. The thickness of the slab should be also small so that the integration of the radiance along z-axis can be approximated by its average at the top and bottom of the layer. This is imperative to be able to solve the discrete, azimuthally averaged transport equation:

$$\mu_i \frac{\partial L(z,\mu_i)}{\partial z} + (\mu_s+\mu_a)L(z,\mu_i) = \\ = \mu_s \sum_{j=1}^{N} \varpi_j \left[h(\mu_i,\mu_j)L(z,\mu_j) + h(\mu_i,-\mu_j)L(z,-\mu_j)\right]. \tag{1.2}$$

Here, the weighting factors ϖ_j are determined by a selected integration procedure. The equation (1.2) can be solved via integration over the thickness, $z_1 - z_0 = \Delta z$, of a thin slab:

$$\mu_i \left[L(z_1,\mu_i) - L(z_0,\mu_i)\right] + (\mu_s+\mu_a)\Delta z L_{1/2}(\mu_i) = \\ = \mu_s \Delta z \sum_{j=1}^{N} \varpi_j \left[h(\mu_i,\mu_j)L_{1/2}(\mu_j) + h(\mu_i,-\mu_j)L_{1/2}(-\mu_j)\right], \tag{1.3}$$

where $L_{1/2}(\mu_i) = 1/2\,(L(z_0,\mu_i) + L(z_1,\mu_i))$ is the average of radiance at the top and the bottom of the slab. The results are expression dependent on the radiance at the top z_0 and bottom z_1, of the

slab, which consequently are the only parameters to be determined. The adding-doubling method is thus mainly used to compute the reflectance and transmittance rather than the fluence inside. The results for a slab, which is twice as thick as the initial slab, are obtained by adding the contributions from each individual slab. This is repeated until the actual physical thickness is reached. The method provides a fast way to go from thin to very thick samples. It applies to problems with inhomogeneous layers and anisotropic scattering.

A formal method to solve a differential equation is to find the solution to its homogeneous part and expand the general solution in terms of the homogeneous solution obtained [30]. This eigenvector - eigenvalue problem has for the transport equation been treated, but has never really been applied to tissue optics. A simpler approach than using the rather complex eigenfunctions, would be to expand the radiance using a well-known appropriate function series. Considering the angular distribution of diffusely scattered light, a realistic choice of orthogonal expansion functions for the diffuse radiance are spherical harmonics. For example, the HG phase function only depends on angle θ or rather $\cos\theta$. An expansion of the phase function into spherical-harmonic function reduces to an expansion into Legendre polynomials:

$$p_{\mathrm{HG}}(\cos\theta) = \frac{1}{4\pi}\frac{1-g^2}{(1+g^2-2g\cos\theta)^{3/2}} = \sum_{n=0}^{N}\frac{2n+1}{4\pi}g^n P_n(\cos\theta), \tag{1.4}$$

where g is the anisotropy and the first Legendre polynomials defined as [39]:

$$\begin{aligned} P_0(x) &= 1, & P_1(x) &= x, \\ P_2(x) &= \frac{1}{2}\left(3x^2-1\right), & P_3(x) &= \frac{1}{2}\left(5x^3-3x\right). \end{aligned} \tag{1.5}$$

A general expression for the phase function can be formulated as an expansion series in Legendre polynomials $P_n(\mathbf{s},\mathbf{s}')$:

$$p\left(\mathbf{s},\mathbf{s}'\right) = \sum_{n=0}^{\infty}\frac{2n+1}{4\pi}b_n P_n(\mathbf{s},\mathbf{s}'), \tag{1.6}$$

where b_n are the expansion coefficients given by

$$b_n = \oint_{4\pi} p\left(\mathbf{s},\mathbf{s}'\right) P_n\left(\mathbf{s},\mathbf{s}'\right) d\Omega'. \tag{1.7}$$

Legendre polynomials $P_n(\cos\theta)$ have proven to be well-suited to axial-symmetric tissue geometry [30, 40]. This implies that the radiance must first be separated into one primary, collimated part, L_c, and one scattered (diffuse) part, L_d:

$$L(\mathbf{r},\mathbf{s}) = L_c(\mathbf{r},\mathbf{s}) + L_d(\mathbf{r},\mathbf{s}). \tag{1.8}$$

Note, that collimated radiance L_c is the collimated light that has not been scattered by the medium. Thus, the collimated part fulfills Beer-Lambert's law:

$$\frac{\partial L_c(\mathbf{r},\mathbf{s})}{\partial s} = -\mu_t L_c(\mathbf{r},\mathbf{s}). \tag{1.9}$$

The diffuse radiance L_d is the part of light that has been scattered at least once. Its angular distribution can be approximated by a truncated series of spherical-harmonic function (Legendre polynomials). For L_d an equation of transfer is only different from the general transfer equation (1.1) in its source term [40]. As collimated light is not scattered, its equation of transfer is equal to:

$$\left[\mathbf{s}\cdot\nabla + (\mu_s+\mu_a)\right] L_c(\mathbf{r},\mathbf{s}) = Q_c\left(\mathbf{r},\mathbf{s}\right), \tag{1.10}$$

where $Q_c(\mathbf{r},\mathbf{s})$ is the collimated part of a light source $Q(\mathbf{r},\mathbf{s})$. Typically, in major OD applications, the light source is located at the surface of the medium (tissue). Thus, it is convenient to introduce the boundary conditions: $Q_c(\mathbf{r},\mathbf{s}) = 0$.

The general RTE for the diffuse radiance L_d is found by substitution of (1.8) into equation of transfer (1.1), and subtraction of (1.10) from the result:

$$[\mathbf{s}\cdot\nabla + (\mu_s + \mu_a)]\, L_d(\mathbf{r},\mathbf{s},t) = \mu_s \oint_{4\pi} p(\mathbf{s},\mathbf{s}')\, L_d(\mathbf{r},\mathbf{s}')\, d\Omega' + \\ + Q_d(\mathbf{r},\mathbf{s}) + \mu_s \oint_{4\pi} p(\mathbf{s},\mathbf{s}')\, L_c(\mathbf{r},\mathbf{s}')\, d\Omega', \quad (1.11)$$

$L_c(\mathbf{r},\mathbf{s}')$ is defined by (1.9), that makes the equation an analogue of the RTE for the total radiance L (1.1) with an extra source term.

The angular distribution of the diffuse radiance L_d can be approximated by a truncated series of Legendre polynomials. Expanding $L_d(\mathbf{r},\mathbf{s})$ into Legendre series with the expansion coefficients $L_n(\mathbf{r})$ similar as it has been done to the phase function (1.6) and (1.7) and substituting it into the (1.1) leads to

$$\sum_{i=0}^{\infty} [\mathbf{s}\cdot\nabla + (\mu_s + \mu_a)]\,(2i+1) L_i(\mathbf{r}) P_i(\mathbf{s}) = \frac{\mu_s}{4\pi} \sum_{j=0}^{\infty}\sum_{k=0}^{\infty} (2j+1) L_j(\mathbf{r})(2k+1) b_k \times \\ \times \oint_{4\pi} \underline{P_j(\mathbf{s}') P_k(\mathbf{s}') d\Omega'} + Q_d(\mathbf{r},\mathbf{s}) + \mu_s \oint_{4\pi} p(\mathbf{s},\mathbf{s}')\, L_c(\mathbf{r},\mathbf{s}')\, d\Omega'. \quad (1.12)$$

The Legendre polynomials are orthogonal over $(-1,1)$ with weighting function 1 and satisfy

$$\int_{-1}^{1} P_i(x) P_j(x) dx = \frac{2}{2i+1}\delta_{ij}. \quad (1.13)$$

Thus, in (1.12) the integral over $d\Omega'$ vanishes, when $j \neq k$:

$$\sum_{i=0}^{\infty} [\mathbf{s}\cdot\nabla + (\mu_s + \mu_a - \mu_s b_i)]\,(2i+1) L_i(\mathbf{r}) P_i(\mathbf{s}) = Q_d(\mathbf{r},\mathbf{s}) + \\ + \mu_s \oint_{4\pi} p(\mathbf{s},\mathbf{s}')\, L_c(\mathbf{r},\mathbf{s}')\, d\Omega', \quad (1.14)$$

and a set of differential equations is finally obtained by multiplying (1.14) by $P_n(\mathbf{s})$. This is followed by another integration over $d\Omega'$. Subsequently, the addition theorem for Legendre polynomials is employed. In the P_N approximation, only N first terms of Legendre polynomial series are taken into account that gives a system of $N+1$ coupled first-order differential equations [14, 29, 30, 34, 40]. The systems can be reduced to a system of coupled second-order differential equations. Finally, the solution for unknowns $L_n(\mathbf{r})$ can be found with the use of a finite-difference or finite-element code.

Diffusion approximation (also known as the P_1 approximation of RTE solution) is an analytical closed-form solution which is suitable for a number of particular problems in various OD applications. With additional assumption of negligible anisotropy in the source, the result is the pair of coupled (time-dependent) equations [12, 14, 18, 34, 41]:

$$\begin{cases} \dfrac{1}{v}\dfrac{\partial \phi(\mathbf{r},t)}{\partial t} + \nabla\cdot\mathbf{J}(\mathbf{r},t) + \mu_a \phi(\mathbf{r},t) = S(\mathbf{r},t), \\ \dfrac{1}{v}\dfrac{\partial \mathbf{J}(\mathbf{r},t)}{\partial t} + \dfrac{1}{3}\nabla\phi(\mathbf{r},t) + \mu_{tr}\mathbf{J}(\mathbf{r},t) = 0, \end{cases} \quad (1.15)$$

where $\phi(\mathbf{r},t)$ and $\mathbf{J}(\mathbf{r},t)$ are the fluence rate and flux at $(\mathbf{r},t)$, and $S(\mathbf{r},t)$ is the photon source:

$$\phi(\mathbf{r},t) = \oint_{4\pi} L(\mathbf{r},\mathbf{s}',t)d\Omega', \quad \mathbf{J}(\mathbf{r},t) = \oint_{4\pi} \mathbf{s}' L(\mathbf{r},\mathbf{s}',t)d\Omega',$$
$$S(\mathbf{r},t) = \oint_{4\pi} Q(\mathbf{r},\mathbf{s}',t)d\Omega'. \tag{1.16}$$

The transport coefficient is defined as $\mu_{tr} = \mu_s' + \mu_a$, where $\mu_s' = \mu_s(1-g)$ refers to the reduced scattering coefficient. The diffusion equation is obtained by eliminating $\mathbf{J}$ between two equations (1.15):

$$\left(\frac{1}{v}\frac{\partial}{\partial t} - D\nabla^2 + \mu_a\right)\phi(\mathbf{r},t) = S(\mathbf{r},t), \tag{1.17}$$

where D is the diffusion coefficient, defined as $D = 1/3\mu_{tr}$.

The radiance in diffusion approximation is expressed as

$$L(\mathbf{r},\mathbf{s},t) = \frac{1}{4\pi}\phi(\mathbf{r},t) + \frac{3}{4\pi}\mathbf{J}(\mathbf{r},t)\cdot\mathbf{s}, \tag{1.18}$$

whereas in most practical diagnostics problems the measurable quantity $R(\rho,t)$ is the number of photons that reach the unit area of a surface in a unit time at given source-detector separation ρ and at given time t. $R(\rho,t)$ defines the diffuse reflectance and is calculated as a current of detected photons across the medium boundary [34, 41]:

$$R_f(\rho,t) = -D\nabla\phi(\rho,z,t)\cdot(-\mathbf{z})|_{z=0}. \tag{1.19}$$

The diffusion equation is a second-order differential equation and its solution is commonly considered for the partial-current boundary conditions, the zero-boundary conditions, and the extrapolated boundary conditions [42, 43, 44]. It has been demonstrated that the solution is more accurate when applied to the reflectance as the integral of the radiance over the backward hemisphere [42, 43]:

$$R(\rho,t) = \iint_{2\pi} \left(\phi(\rho,z,t) + 3D\frac{\partial\phi(\rho,z,t)}{\partial z}\right)\Bigg|_{z=0} (1 - R_{Fres}(\theta))\,\frac{d\Omega}{4\pi}, \tag{1.20}$$

where $R_{Fres}(\theta)$ is the Fresnel reflection coefficient for incident light at angle θ relative to the normal to the medium boundary. For the extrapolated boundary condition and having employed the method of image sources to solve the diffusion equation for fluence rate ϕ within the medium lead to [45]:

$$\phi(\rho,z,t) = \frac{v}{(4\pi Dvt)^{3/2}}\exp(-\mu_a vt)\left\{\exp\left[-\frac{(z-z_0)^2+\rho^2}{4Dvt}\right] - \right.$$
$$\left. - \exp\left[-\frac{(z+z_0+2z_b)^2+\rho^2}{4Dvt}\right]\right\}. \tag{1.21}$$

The first term is due to a point source at $z_0 = (\mu_{tr})^{-1}$ that results from the perpendicularly incident collimated light, and the second one is due to a negative image source at $-z_0 - 2z_b$. The fluence rate is set to zero at the extrapolated boundary located at z_b

$$z_b = \frac{1+R_{eff}}{1-R_{eff}}2D. \tag{1.22}$$

Here, R_{eff} represents the fraction of photons that have been internally diffusely reflected at the medium boundary.

According to [42]:

$$R_{eff} \equiv \frac{R_\phi + R_j}{2 - R_\phi + R_j}.$$

$$R_\phi \equiv \int_0^{\pi/2} 2\sin\theta\cos\theta R_{Fres}(\theta)d\theta, \quad R_j \equiv \int_0^{\pi/2} 3\sin\theta\cos^2\theta R_{Fres}(\theta)d\theta. \tag{1.23}$$

It is possible to regroup (1.20) and express it in terms of conventional expression for ϕ (1.21) and $R_f(\rho,t)$ (1.19) [42, 43]:

$$R(\rho,t) = \underbrace{\frac{1}{2}\left(\frac{1}{2} - \frac{R_\phi}{2}\right)}_{C_\phi}\phi(\rho,t) + \underbrace{\frac{1}{2}(1-R_j)}_{C_j}R_f(\rho,t). \tag{1.24}$$

The derivation of the diffusion equation as it has been shown above is not unique. Some other approaches, all assuming isotropic scattering, such as a random walk, elementary kinetic theory (e.g. [46]) are known. These approaches do not necessarily provide the same expression for the diffusion coefficient D. There is a number of studies discussing an exact expression for D [41, 46, 47] as well as a number of models have been proposed, trading off accuracy for computational ease [2]. The main limitation of the diffusion approximation is that the distance between sources and detectors should be much greater than the mean transport length so that enough scattering events occur to generate a diffuse field [48, 49]. Additionally, the source and detector sizes must be small enough as compared to the distance of their separation. The diffusion approximation is also not valid for photons with short arrival time ("snake" or low-order scattering photons) to the detector [50].

Stochastic models are an alternative to deterministic models and have been developed to model light transport in biological tissues [34, 51]. Stochastic methods proceed in a very different way from deterministic methods. These methods involve modeling of individual photon interactions either implicitly, i.e. by deriving the probability density functions for photons transitions. The problem of light transport through a scattering medium like a biological tissue is considered to be probabilistic in nature for two reasons. Firstly, at the level of individual photons, light scattering is a probabilistic phenomenon governed by the laws of quantum mechanics. Secondly, considering light intensities averaged over a larger number of photons, the nature of the scattering medium itself is random due to the large variety in distribution, shape and orientation of the scattering centers.

Random walk theory (RWT) describes the statistical behavior of light propagation in scattering medium, constrained along the elements of a discrete lattice. RWT is based on two assumptions: the tissues continuum is replaced by a cubic lattice with a step size inversely proportional to the scattering coefficient, and that photons move isotropically between adjacent lattice points which significantly restricts the number of possible photon directions [52, 53]. The derived functions are the joint probabilities that a photon emerges at distance ρ on surface after n lattice steps, where ρ measures the axial distance from the point of insertion to the point of re-emission. For a finite slab, one can derive the joint probabilities in reflection and transmission after taking into account appropriate boundary and initial conditions. Time-dependent expressions have been derived for a homogeneous scattering medium and are in a good agreement with the results of diffusion theory. Anisotropy for the case of continuous-wave and time-resolved measurements for both reflectance and transmission modes was introduced in [54]. The advantage of RWT is the ability to produce relatively simple mathematical expressions for various quantities of interest such as diffuse reflectance and transmittance. The disadvantage includes a constant lattice step, that makes difficult an application of the model of a layered medium. All resulting restrictions, similar to those for the diffusion approximation, are also valid for RWT.

Photon path-integral formalism The RTE describing light propagation can be interpreted as a collection of photon paths taken by radiation as it travels in the medium, $\mathbf{r}(t)$. Thus, a path

integral (PI) $P[\mathbf{r}(t)]$ is an integral over all such possible paths traveled by photons. Optical fields are described using the concept of an ensemble of effective optical paths of partial contributions [55, 56, 57]. PI methods analytically find the most important paths and develop quantitative estimates based on them. The multiple scattering contributions are only computed along the most probable paths and the rest of the paths are dealt with implicitly via analytic integration of multiple scattering. This technique has been experimentally verified [58]. The great virtue of the PI approach is the huge computational saving it affords by making systematic, rather than random, searches through photon histories. Hence, the PI formalism offers analytic solutions to the RTE without using the diffusion approximation, and it is well suited to describing the propagation of both early-arriving and fully-diffused photons. The number of studies on this subject is still quite limited [59, 60] and practical implementations are confined to a few publications [55, 58].

1.2 Monte Carlo Method

The Monte Carlo (MC) method is a prominent example of stochastic methods that stand alone when analytic approaches have difficulties in giving a satisfactory solution. In this probabilistic technique, the trajectories of individual multiple scattered photons are traced through the media, each interaction being governed by random processes of scattering and absorption. Due to the lack of intrinsic constraints, facing the problem of combining computation complexity of light propagation model and ability to cope with the optical parameters of biological tissues, which are anticipated to vary spatially and temporally as well as individually, MC technique is chosen as a primary tool for modeling of optical radiation propagation in biological tissues by many researchers [2, 38, 61–69].

The basic assumption of MC is that the process of photon migration is considered as a sequence of random non-correlated events or Markov process [61, 71, 72]. In case of light propagation this means that the probability that a photon will change from its present state to another state is independent of its previous states, i.e. it has no awareness of its previous history. For scattering, for this to be true, the scattering particles will have to be distributed non-periodically (a regular lattice would produce a diffraction pattern), and the light should be non-coherent so that interference effects are typically ignored.

In case of radiative transfer in biological tissue, the MC method is a method to estimate the exact solution of RTE. This is done by sampling the set of all possible paths of photon packets (or photons) through the tissue. In a simple case the random paths of a large number of photon packets are simulated. The expected value of a random or stochastic variable can be seen as the integral over all possible values of that variable multiplied by their probabilities. Estimation of an expected value using the MC method is thus a form of a numerical quadrature. Indeed, the RTE (stationary form in a homogeneous medium) can be written as an integral equation [30]:

$$L(\mathbf{r},\mathbf{s}) = \int_{\mathrm{R}=0}^{\infty} \exp\left(-\mu_{tr}\mathrm{R}\right)\mu_s \int_{4\pi} p\left(\mathbf{s},\mathbf{s}'\right) L(\mathbf{r}-\mathrm{R}\mathbf{s},\mathbf{s}')d\Omega' d\mathrm{R} + \int_{\mathrm{R}=0}^{\infty} \exp\left(-\mu_{tr}\mathrm{R}\right) Q(\mathbf{r}-\mathrm{R}\mathbf{s},\mathbf{s})d\mathrm{R}. \quad (1.25)$$

Here, the radiance L at position $\mathbf{r}$ in direction $\mathbf{s}$ originates from the light source and from the radiance scattered elsewhere into direction $\mathbf{s}$; R is a path length. The second term defines light in direction $\mathbf{s}$ that originates from source Q at positions $\mathbf{r}-\mathrm{R}\mathbf{s}$, that survives the transfer from positions $\mathbf{r}-\mathrm{R}\mathbf{s}$ to position $\mathbf{r}$, by factor $\exp\left(-\mu_{tr}\mathrm{R}\right)$. The first integral term represents light that has been

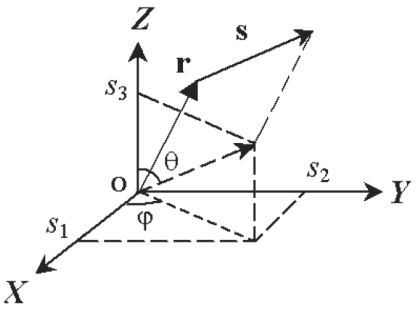

Figure 1.3: The Cartesian coordinate system (XYZ) is employed to specify the position $\mathbf{r}$ of a photon in the modeling medium: angles θ and φ are the polar and azimuth angles which define $\mathbf{s}$, the direction of photon packet propagation. s_1, s_2, s_3 are the direction cosines.

scattered at positions $\mathbf{r} - R\mathbf{s}$, from direction $\mathbf{s}'$ into direction $\mathbf{s}$, that also reached position $\mathbf{r}$.

1.2.1 Implementation of Monte Carlo simulation

Photon packets propagate through scattering matter. The points where interactions with the matter occur are described by *probability density function* (pdf). If x is a variable that characterizes the interaction (e.g. scattering angle or distance), its pdf $p(x)$ is defined as:

$$\int_{-\infty}^{\infty} p(x)dx \equiv 1 \qquad F(x) = P(x \le a) \equiv \int_{-\infty}^{a} p(x)dx, \tag{1.26}$$

where $F(x), 0 \le F(x) \le 1$ is the cumulative probability function (cpdf). $F(x)$ is equal to a probability $P(x \le a)$ that a random variable x is less than a. By taking the inverse, F^{-1} the random samples can then be obtained from this function by the use of random numbers ξ uniformly distributed between 0 and 1 according to [71]:

$$\xi = \int_{-\infty}^{x} p(x)dx \qquad \rightarrow \qquad x = F^{-1}(\xi). \tag{1.27}$$

There are also other techniques such as rejection sampling or table-lookup method that can be used for the same purpose [71].

The photon's phase space $\{\mathbf{r}, \mathbf{s}\}$ is the collection of dynamic variables that describe the photon's absolute location in the medium referred to the coordinate system, $\mathbf{r}$, and its direction, $\mathbf{s}$, referred back to fixed set of axes in the same coordinate system (Fig. 1.3). The coordinate system is usually the one where the fixed components of the experiment resides. $\mathbf{r}$ represents the 3-component vector $\mathbf{r} = (x, y, z)$, and $\mathbf{s}$ represents the 3-component vector $\mathbf{s} = (s_1, s_2, s_3)$. The direction of incident photons is specified by the initial polar angle θ and azimuthal angle φ and the components of the vector $\mathbf{s}$ are often referred to the direction cosines, $\{s_1, s_2, s_3\} = \{\sin\theta\cos\varphi, \sin\theta\sin\varphi, \cos\theta\}$.

A photon packet phase space can be supplemented with other variables, such as intensity, polarization, etc. In simple MC simulation statistic weight of a photon packet is introduced into the phase space to characterize the photon packet contribution to the variable of interest, e.g. reflectance or transmittance.

In its phase space the photon packet is represented by the pdf, which is dependent on space coordinates, direction cosines, and the statistical weight. The simulation is based on the modeling

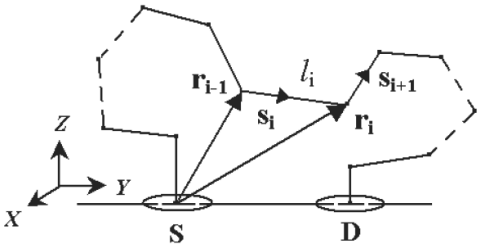

Figure 1.4: Schematic presentation of a photon packet propagation in a scattering medium. l_i is the photon packet path length between $i-1$-th and i-th scattering centers located at $\mathbf{r}_{i-1}$ and $\mathbf{r}_i$. Unit vectors $\mathbf{s}_i$ and $\mathbf{s}_{i+1}$ define the direction of photon packet propagation prior to and straight after the scattering event.

of a large number of possible trajectories of the photon packets from the site of the photons' injection into the medium (source) to the site, where the photons leave the medium (detector) (Fig. 1.4).

The pdf can be factorized as a product of three independent pdfs, i.e. the pdf of position, the pdf of scattering, the pdf of importance, reflecting the physical fact that the spatial, directional and importance distributions are *mutually independent* from each other. Hence, an individual trajectory of a photon packet is modeled as a sequence of the following elementary simulations: i) generation of photon path lengths, ii) simulation of scattering event, iii) reflections/refractions on the medium boundaries, iv) absorption events, v) fluorescence events, vi) an act of Raman scattering, etc. for particular OD applications. The initial and final states of the photons are entirely determined by the source and the detector geometries and numerical apertures.

1.2.2 Transfer of a photon packet in the medium

Assume the trajectory of a photon packet consists of i points with coordinates given by $\mathbf{r}_k$, $k=\overline{1..i}$. Given that a photon packet has a direction $\mathbf{s}_i$ and a distance l_i to travel, the new position $\mathbf{r}_i$ is given by:

$$\mathbf{r}_i = \mathbf{r}_{i-1} + \mathbf{s}_i l_i. \tag{1.28}$$

The distance l_i (or l for brevity) is referred to a free path length, and is determined according to the corresponding pdf.

$$l = -\frac{\ln \xi}{\mu_s}, \tag{1.29}$$

where ξ is a uniformly distributed random number between 0 and 1.

Path length distribution $p(l)$ can take on any positive values [72]:

$$p(l) = \mu_t \exp(-\mu_t l) = \mu_s \exp(-\mu_s l)\exp(-\mu_a l) + \mu_a \exp(-\mu_a l)\exp(-\mu_s l), \tag{1.30}$$

where $\mu_t = \mu_s + \mu_a$ is the extinction coefficient. The first term in (1.30) describes photon scattering, along with its reduction due to the absorption in a medium, $\exp(-\mu_a l)$. The second term determines photon absorption in the medium. For the major OD applications, the main interest lies in the detection of photon packets by a particular detector, rather than calculating the fraction of the incident photons that have been absorbed in a medium. Factorizing the first term into the product of the pdf of scattering, $p_s(l)$ and attenuation factor, $\exp(-\mu_a l)$, it is seen that the acts of scattering and absorption can be modeled independently, i.e.:

$$p(l) = p_s(l)\exp(-\mu_a l) \tag{1.31}$$

and

$$p_s(l) = \mu_s \exp(-\mu_s l). \tag{1.32}$$

The procedure of selection of l becomes more complicated if the medium is heterogeneous. Leaving the problems associated with boundary interactions, the attention is drawn to variation of a free path length of a photon packet due to transition into a region with different scattering coefficients. Consider n regions with the scattering coefficients μ_{sk}, $k = \overline{1..n}$. If the photon packet crosses the distances l_k, in these regions, then the pdf (1.32) is defined as [71]:

$$\begin{gathered} p_s(l) = \mu_{sj} \exp\left[-\left(\sum_{k=1}^{j-1} \mu_{sk} l_k \right) - \mu_{sj} \left(l - \sum_{k=1}^{j-1} l_k \right) \right], \\ \text{provided that} \qquad \sum_{k=1}^{j-1} l_k \le l \le \sum_{k=1}^{j} l_k. \end{gathered} \tag{1.33}$$

Note that l_j is a maximum possible distance that a packet can cross in the j-th region. Thus, the path length selection can be carried out by determining j from the inequalities:

$$\sum_{k=1}^{j-1} \mu_{sk} l_k \le -\ln \xi \le \sum_{k=1}^{j} \mu_{sk} l_k \tag{1.34}$$

and then calculating

$$l = \sum_{k=1}^{j-1} l_k + \frac{1}{\mu_{sj}} \left(-\ln \xi - \sum_{k=1}^{j-1} \mu_{sk} l_k \right). \tag{1.35}$$

The implementation of (1.35) is not straightforward as the distances l_k are not known. Instead of this, a step-by-step procedure is applied [69]. If a boundary demarcating a region of space with different scattering coefficients the path length that the packet has traveled in the region $k-1$ is subtracted from the total path length l, i.e. $l^* = l - l_{k-1}$. Based on (1.35), the remaining step l^* to be traveled in region k has to be converted in accordance with the new scattering coefficient:

$$l^{**} = l^* \frac{\mu_{s(k-1)}}{\mu_{sk}}. \tag{1.36}$$

This procedure repeats until the path length l^{**} is not long enough to intersect the interface of the adjacent layer. If a void region, i.e. $\mu_{sk} = 0$, is encountered in the course of propagation, the photon packet is moved directly to the next adjacent boundary following its direction.

The photon packet path length l to next interaction can be sampled by considering the medium as uniform in terms of the local scattering coefficient. If the medium consists of inhomogeneities with different scattering coefficients the photon packet is stopped at that boundary and its path length l is truncated at that boundary. The next free path is taken from that boundary point with the scattering coefficient being that of the region beyond the boundary. Other possible techniques can be found in [71].

1.2.3 Scattering

Variations of refractive index are responsible for light scattering in tissues. The refraction variations are determined by the biochemical makeup of the tissue and will influence the amplitude of the scattered light. In terms of tissue morphology, the relative size of organelles and cells with respect to the wavelength of incident light affects the angular distribution of the scattered light. Increasing difference in the index of refraction between the cell components and surrounding result in an increasing scattering of the medium [2]. Mammalian cells range from 10 to 30 μm in diameter, and

TABLE 1.1: The average cellular constituents and their scattering properties, collected from [2] and references within.

Structure	Diameter, μm	n	Shape	Scattering properties
Red Blood Cell	8.5	1.40	disk	Mie
Mitochondria	1	1.38-1.41	cylindrical	Mie
Nucleus	7	1.39-1.47	spherical	Mie
Lysosomes	0.25-0.8		spherical	Mie
Endoplasmic reticulum	few		folded sheets	Mie + Rayleigh
Microtubules & filaments		1.5		Rayleigh
Golgi apparatus		1.5		Rayleigh
Cytosol		1.354		

their internal organelles appear in a broad assortment of shapes and sizes. Table 1.1 lists the most common cellular organelles inside mammalian cells.

Although the cytoplasmic components such as Golgi apparatus, lysosomes, endoplasmic reticulum, mitochondria, etc., appear to be greatly different in their structure and organization [73, 74], a few generalizations can be made: a) most of cytoplasmic organelles and inclusions are smaller than 1 μm in size; b) they are not homogeneous bodies but rather complex structures. Typical nuclei size ranges from 5 to 10 μm and like other cell organelles, nuclei are not a uniform object and have a complex internal structure. The cell mainly contains an aqueous solution of electrolytes and proteins, the cytoplasm, with an effective refractive index of approximately 1.38, while the cell membrane and cell organelles are composed of phospholipid layers and proteins with refractive indices in the range of 1.43-1.51 [25]. However, since the fraction of these higher refractive index components is rather small, i.e. in the order of 5%, the effective cellular refractive index can be estimated to ~ 1.40. When studying the spatial variations in the refractive index over a microscopic scale such as the inside of a cell using a phase microscope, it is found that the cell membrane and the nucleus are the components which are the dominant contributions to the cellular effective refractive index; these are far more important than, for example, the mitochondria. This does not mean, however, that the membrane and the nucleus are the main scatterers in tissue. Apart from the refractive index, parameters such as structure, size and concentration of the scattering object must also be taken into account. For instance, the cell membrane has a thickness of only 5-10 nm and thus has a relatively insignificant effect on the total light scattering from the cell, despite its high refractive index. Instead, a high correlation between the reduced scattering coefficient and the mitochondrial content has been found [75]. Tissues of high mitochondrial content exhibit high scattering coefficients. Light scattering from tissues with high concentrations of mitochondria such as liver tissue, can to large extent (but far from completely) be attributed to this organelle despite its low refractive index. The basic lipid bilayer membrane is about 9 nm in width. The refractive index mismatch between lipid and the surrounding aqueous medium causes strong scattering of light. Folding of lipid membranes presents larger size lipid structures which affect longer wavelengths of light. The density of lipid/water interfaces within the mitochondria make them especially strong scatterers of light. Lipid droplets inside the cells of adipose tissue have been shown to be a major contributor to the cellular scattering, due to their high refractive index and high volume fraction (88%) in the cell [75]. The strong scattering characteristics of lipid particles is further confirmed by the high correlation found between the lipid content of liver tissue and the reduced scattering coefficient [76], when the influence of the mitochondrial content has been compensated for.

Apart from cellular components, connective tissue fibers are found to be responsible for scattering [77, 78]. It was shown that scattering in neonatal skin is mostly dominated by Mie scattering from cylindrical collagen fibers [79]. The refractive index of collagen has been measured to be between 1.46 and 1.55 [80]. Rayleigh scattering was also presented emerging mostly from collagen fibrils, which are much smaller and do not bundle. S. Jacques [78] has attributed scattering of soft tissues in the near-infrared region to membraneous structures that were modelled as spherical Mie scatterers in 0.2–2 μm diameter range. Table 1.1 gives some insight into the nature of scattering from cellular constituents.

Detailed theoretical information on the light scattering from specific cells and their organelles can be obtained by utilizing the various methods based on electromagnetic theory [2, 81]. The general results for such computations show that small scatterers, compared to wavelength, yield essentially isotropic scattering, whereas particles of greater size exhibit more pronounced forward scattering. Mie computations utilizing a cylindrical-particle model can also be applied to investigate the influence of the size of an elongated scattering object such as collagen fibers on the light scattering [79]. Correspondingly, thin (compared to wavelength) fibers yield scattering with isotropic character, whereas enlargement, as observed for instance due to maturity of collagen fibers in neonatal skin, increases the anisotropy and the scattering cross section.

Although contribution to the total cellular scattering from the nucleus is relatively small, changes in its size and refractive index influences the angular distribution of the scattered light. RGD computation of a layered sphere model with a particle size in the order of a lymphocyte (a type of white blood cell) ($\sim$ 8-10 μm), reveals that an increased nucleus diameter, at constant total cell size, increases the forward scattering. This is supported by results of finite-difference time-domain computations [82], however, the decrease of refractive index of either nucleus or the surrounding cytoplasm causes a decrease in the forward scattering [82].

Experimental evidence supports the hypothesis that light scattering in biological tissues is anisotropic with significant forward scattering, $g \simeq 0.7$–0.97 [83]. Goniometer measurements of a number of animal model tissues indicate that g as a function of wavelength is approximately 0.9 with a tendency to increase with wavelength. Similar values of the anisotropy factor g in the range of 0.7–0.95 for skin tissue in the visible spectral range have been reported in [84]. Forward-peaked scattering functions for human stratum corneum and epidermis at ultraviolet and visible wavelengths has been demonstrated in [85]. Values of g between 0.71 at 300 nm and 0.78 at 540 nm, varying linearly with wavelength have been presented in [86]. With the full thickness epidermis, the distribution of the transmitted light also peak, although less strongly than with stratum corneum.

It has been shown in [86] that a least squares fit identifies the Henyey-Greenstein (HG) phase function as a good choice for describing scattering behavior in the stratum corneum. The HG scattering phase function, an empirical approximation for Mie scattering from particles with a distribution of sizes [87], is defined as

$$p_{HG}(\cos\theta) = \frac{1}{4\pi} \frac{1-g^2}{(1+g^2-2g\cos\theta)^{3/2}} \tag{1.37}$$

where θ is the scattering angle.

It should be pointed out that since the epidermis is very thin and because its micro-structure composed of keratin fibers is analogous to the collagen fibers of the dermis, dermal scattering can be used to approximate skin scattering. The refractive index ratio between stratum corneum and air is about 1.51 [88–90]. This gives rise to surface scattering, which follows the Fresnel's equations [24] and is affected by the presence of folds in stratum corneum. The influence of stratum corneum fold structure on the detected optical signal localization in biological tissues has been discussed in [91].

The photon packet is scattered at the scattering center and a new direction of the packet is determined relative to the origin of photon direction (Figure 1.5). The coordinate system (XYZ) contains

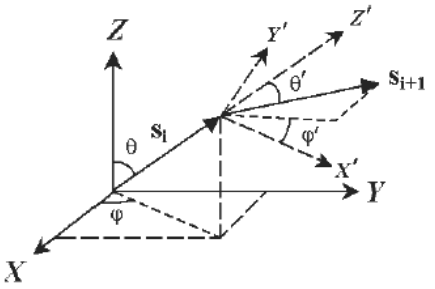

Figure 1.5: A new direction defined in local coordinate system $(X'Y'Z')$ by the deviations in the polar angle θ' and azimuthal angle φ' in terms of the coordinate system (XYZ). Unit vectors $\mathbf{s}_i$ and $\mathbf{s}_{i+1}$ define the direction of photon packet propagation prior to and straight after scattering.

the absolute initial direction $\mathbf{s}_i$. New direction $\mathbf{s}_{i+1}$ is originally defined in local coordinate system $(X'Y'Z')$ by the deviations in the polar angle θ' and azimuthal angle φ', relative to the previous direction. In the coordinate system $(X'Y'Z')$ a new direction $\mathbf{s}_{i+1}$ is given by the direction cosines $\{\sin\theta'\cos\varphi', \sin\theta'\sin\varphi', \cos\theta'\}$. In XYZ a new direction $\mathbf{s}_{i+1}$ and the corresponding direction cosines $\{s_{1i+1}, s_{2i+1}, s_{3i+1}\}$ are defined as [61, 70, 92–94]:

$$\begin{pmatrix} s_1 \\ s_2 \\ s_3 \end{pmatrix}_{i+1} = \begin{bmatrix} \dfrac{s_{1i}s_{3i}}{\sqrt{1-s_{3i}^2}} & -\dfrac{s_{2i}}{\sqrt{1-s_{3i}^2}} & s_{1i} \\ \dfrac{s_{2i}s_{3i}}{\sqrt{1-s_{3i}^2}} & \dfrac{s_{1i}}{\sqrt{1-s_{3i}^2}} & s_{2i} \\ -\sqrt{1-s_{3i}^2} & 0 & s_{3i} \end{bmatrix} \begin{pmatrix} \sin\theta'\cos\varphi' \\ \sin\theta'\sin\varphi' \\ \cos\theta' \end{pmatrix}, \tag{1.38}$$

where $\mathbf{s}_i = \{s_{1i}, s_{2i}, s_{3i}\}$ are the direction cosines before the i-th scattering. If $|s_{3i}|$ is too close to 1, the photon is assumed not to deflect, and

$$\begin{pmatrix} s_1 \\ s_2 \\ s_3 \end{pmatrix}_{i+1} = \begin{pmatrix} \sin\theta'\cos\varphi' \\ \sin\theta'\sin\varphi' \\ \dfrac{s_{3i}}{|s_{3i}|}\cos\theta' \end{pmatrix}. \tag{1.39}$$

The values of deviations are determined from the corresponding cpdfs: $\theta' = F_{\theta'}^{-1}(\xi)$ and $\varphi' = F_{\varphi'}^{-1}(\xi)$ (see 1.27). The HG scattering phase function p_{HG} is typically used. The phase function is effectively the pdf of scattering and fulfills all requirements for pdf (1.27). p_{HG} is factorized as follows:

$$\begin{gathered} p_{HG} = p_{\theta'}(\theta')p_{\varphi'}(\varphi'), \\ p_{\theta'}(\cos\theta') = \frac{1}{2}\frac{1-g^2}{(1+g^2-2g\cos\theta')^{3/2}}, \quad p_{\varphi'}(\varphi') = \frac{1}{2\pi}. \end{gathered} \tag{1.40}$$

The cpdf of $p_{\theta'}(\cos\theta')$, $F_{\theta'}(\cos\theta')$, is given by

$$F_{\theta'}(\cos\theta') = \frac{1}{2g}\left(\frac{1-g^2}{\sqrt{1+g^2-2g\cos\theta'}} - (1-g)\right) \tag{1.41}$$

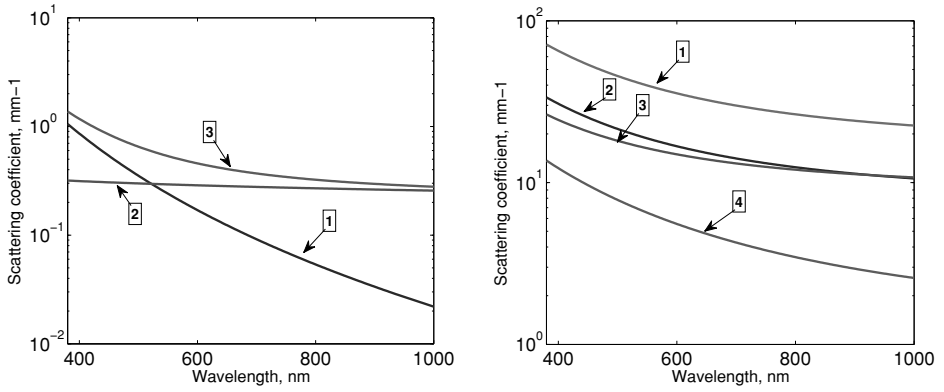

Figure 1.6: Reduced scattering coefficient of human skin (a) suggested in [79], where: 1 - Rayleigh scattering, 2 - Mie scattering by collagen fibers, 3 - the combined Rayleigh and Mie scattering; scattering properties of tissues used in the simulation (b), where: 1 - stratum corneum; 2 - living epidermis; 3 - papillary dermis; 4 - upper blood net dermis; 5 - reticular dermis; 6 - deep blood net dermis; 7 - subcutaneous fat.

Applying transformation (1.27), the choice for $\cos\theta'$ and φ' can be expressed as follows:

$$\begin{aligned} \cos\theta' &= \begin{cases} \dfrac{1}{2g}\left(1+g^2-\left[\dfrac{1-g^2}{1-g+2g\xi}\right]^2\right), & \text{if } g>0 \\ 2\xi-1, & \text{if } g=0. \end{cases} \\ \varphi' &= 2\pi\xi. \end{aligned} \tag{1.42}$$

Note, any other scattering phase function can be used, instead of the HG function. If analytical inversion, see (1.27) and (1.41), is not possible, then the table lookup method is invoked [71, 95, 96]. According to this method, points within equally probable intervals of the variable to be selected are picked up randomly from a pre-calculated table of the inversed cpdf of the variable similar to (1.26). The cpdf for the scattering angle θ' or rather $\cos\theta'$ can be numerically constructed:

$$F(\cos\theta') = \int_{-1}^{\cos\theta'} p(\cos\theta)d\cos\theta, \quad F(1)=1. \tag{1.43}$$

The inverted cpdf, $icpdf = F^{-1}(\cos\theta')$, containing values of $\cos\theta'$, can be calculated and stored in the array $icpdf[k]$, $k = \overline{1..\max(k)}$. For all k the two values, $cpdf[k-1]\cdot\max(k)$ and $cpdf[k]\cdot\max(k)$ that most closely correspond to the index value k are looked up in the array $cpdf[k]$. Notice that $\max(cpdf[k]) = 1$ and $\min(cpdf[k]) = 0$ (1.26). Lagrange polynomial or any other and appropriate interpolation technique is performed to find the best approximate value. Finally, the array $icpdf[k]$ filled with equally probable values of $\cos\theta'$ obeying the assumed pdf, is constructed. The usage of the table is straightforward.

A generated random number ξ is re-scaled to span over the entire array $icpdf[k]$, i.e. simply multiplied by $\max(k)$, and is used to find corresponding index k^*, such that $k^*-1 \le \max(k)\xi \le k^*$. Again, Lagrange interpolating polynomials are used to find the value $\cos\theta'$ corresponding to $\max(k)\xi$.

The approximated scattering coefficients of human skin layers based on a combination of Mie and Rayleigh theories are presented in Fig. 1.6 and were obtained from a number of sources ([2, 78, 79, 97, 98, 99]).

1.2.4 Absorption

There are two major assumptions which are used in the modeling of tissue absorption. The first assumption is that absorption occurs at discrete sites corresponding to the position of scattering and absorbing centers (see Fig. 1.2 b). The advantage of this method is that it is relatively easy to keep the track of the absorbed dose in the tissue [63, 64, 69, 100]. Absorption is modeled by terminating a photon packet in an unbiased way by comparing a random number with a single scattering albedo, $\frac{\mu_s}{\mu_s+\mu_a}$. If a random number is less than albedo, scattering occurs, otherwise absorption takes place [66]. However, this will result in a rapid death of a packet, and consequently long computational time. To avoid this a photon packet is attributed with the statistical weight W [71]. During the course of photon packet propagation, the weight W will be decreasing, that is understood as the absorption.

We consider the model when absorption takes place along the path of the photon packet. This approach corresponds to the tissues model presented by an ensemble of scattering centers in an absorbing continuum. The same assumption has been favored in a number of studies, where the optical radiation detected on the surface of the medium is of interest [67, 101, 102, 103, 104]. A combination of both methods can be used to account absorption of discrete particles and absorbing background [105]. The implication of this approach is that for the photons that have passed through a heterogeneous medium with regions of different absorption coefficients, μ_{ak}, $k = \overline{1..n}$.

Absorption is modeled in the similar manner (1.31), by attenuation of the statistical weight of a photon packet:

$$W_d = W_0 \exp\left(-\sum_k \mu_{ak} l_k\right), \tag{1.44}$$

where W_d is the weight of the detected photon packet, and W_0 is the initial weight of the photon packet, typically equal to 1. Intensity of the exiting radiation is given by:

$$I_d = I_{in} \exp\left(-\sum_k \mu_{ak} l_k\right), \tag{1.45}$$

where I_d is the intensity observed at detector, and I_{in} is the intensity of incident radiation, l_k is the total path length in the k-th region in the medium.

Thus, the photon packet represents a group of many photons, and is a part of photons initially injected into the medium. At each point of the trajectory the weight of the group of photons is equal to the number of unabsorbed photons which represents the probability to reach this point along the trajectory. The statistical weight W_d of each stored photon is counted by:

$$W_d = W_0 (1 - R_{in}) \left[\prod_{p=1}^{M} R^*\right] (1 - R_{out}) \exp\left(-\sum_k \mu_{ak} l_k\right). \tag{1.46}$$

Notice that the absorption μ_{ak} does not influence the photon histories. The separate simulation of the scattering and absorption agrees with the Beer-Lambert law and allows the rapid recalculation of the probing radiation intensity on the detector domain for a set of the medium absorption coefficients without re-calculation of trajectories of photon packets.

Two major tissue layers are conventionally recognized as comprising human skin, i.e. epidermis and dermis (Figure 1.7). The outer, most superficial, layer is the epidermis that varies relatively little in thickness over most of the body, between 75 and 150 μm, apart from on the palms and foot

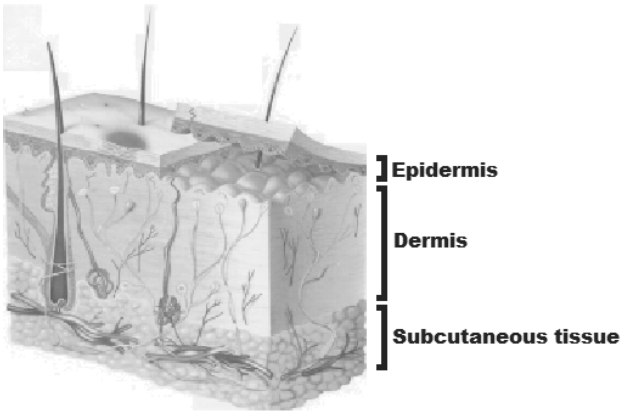

Figure 1.7: Schematic presentation of human skin structure.

soles, where the thickness can be 0.5 mm [106]. The dermis lying beneath the epidermis is a dense elastic connective tissue that constitutes the principal mass of the skin. There is a considerable variation in the thickness of the dermis, an average thickness is 1–2 mm [107]. Underlying the skin is subcutaneous (under-the-skin) tissue, or hypodermis, an average thickness is 1–2 mm.

For MC simulations the extended multi-layer skin model developed in [108] is used. Table 1.2 presents a summary of the typical optical properties of skin tissue layers collected from a number of sources [68, 72, 84, 86, 88–90, 97, 99, 107, 109–116].

TABLE 1.2: Typical optical properties of human skin.

	Skin layer	μ_s, mm^{-1}	μ_a, mm^{-1}	g	n	t, μm.
1	Stratum corneum	80-100	0.1	0.8-0.9	1.5-1.55	10-20
2	Living epidermis	35-60	0.15	0.8-0.85	1.34-1.4	80-100
3	Papillary dermis	30-35	0.068	0.8-0.9	1.39	150-200
4	Upper blood net dermis	25-27	0.095	0.9-0.95	1.4	80-100
5	Reticular dermis	20-25	0.073	0.76-0.8	1.39-1.4	1150-1500
6	Deep blood net dermis	30-35	0.118	0.95	1.38-1.4	80-120
7	Subcutaneous fat	5-15	0.068	0.75-0.8	1.44	5000-6000

The absorption of skin layers takes into account concentration of blood (C_{blood}) in various vascular beds, oxygen saturation (S), water content (C_{H2O}), melanin fraction (C_{mel}), and is defined as [108]:

$$\mu_a^{Strat.corneum}(\lambda) = (1 - C_{H_2O})\mu_a^{baseline}(\lambda) + C_{H_2O}\mu_a^{water}(\lambda) \tag{1.47}$$

$$\mu_a^{Living\,epidermis}(\lambda) = (1 - C_{H_2O})\left[C_{mel}(B_{mel}\mu_a^{mel}(\lambda) + (1 - B_{mel})\mu_a^{ph.mel}(\lambda)) + (1 - C_{mel})\mu_a^{baseline}(\lambda)\right] + \\ + C_{H_2O}\mu_a^{water}(\lambda) \tag{1.48}$$

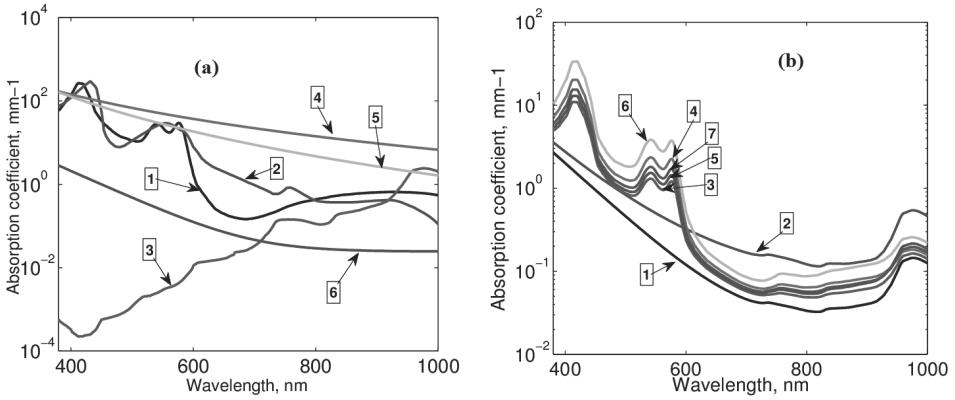

Figure 1.8: Absorption coefficients of key skin tissues chromophores (a), where: 1 - oxy-hemoglobin, 2 - deoxy-hemoglobin, 3 - water, 4 - eumelanin, 5 - pheomelanin, 6 - baseline; Absorption coefficients of the human skin layers (b) counted by equations (1.47), (1.48), (1.49).

$$\begin{aligned}\mu_a^{Dermis}(\lambda) = (1-C_{H_2O})\left[(C_{blood}F_{Hb}F_{RBC}Ht)(S\mu_a^{oxy}(\lambda)+(1-S)\mu_a^{deoxy}(\lambda))\right]+\\ +(1-C_{H_2O})\left[(1-C_{blood}F_{Hb}F_{RBC}Ht)\mu_a^{baseline}(\lambda)\right]+\\ +C_{H_2O}\mu_a^{water}(\lambda)\end{aligned} \tag{1.49}$$

Here ${\mu_a}^{mel}(\lambda)$ is the absorption coefficient of eumelanin, ${\mu_a}^{ph.mel}(\lambda)$ is the absorption coefficient of pheomelanin, B_{mel} is the volume fraction of the blend between two melanin types, ${\mu_a}^{oxy}(\lambda)$ is the absorption coefficient of oxy-hemoglobin, ${\mu_a}^{deoxy}(\lambda)$ is the absorption coefficient of deoxy-hemoglobin, ${\mu_a}^{baseline}(\lambda)$ is the absorption coefficient of other water-free tissues, Ht is the hematocrit, F_{Hb} is the volume fraction of hemoglobin, F_{RBC} is the volume fraction of erythrocytes. The absorption of the main skin chromophores and skin layers are summarized in Figure 1.8.

Blood and water content in the layers of human skin is presented in Table 1.3 and is collected from a wide range of literature [72, 77, 107, 117–121].

Total hemoglobin volume fraction in blood γ is calculated assuming that hemoglobin is contained in the erythrocytes only, i.e. $\gamma = F_{Hb}F_{RBC}Ht$. Here $Ht = 0.45$ is the hematocrit, the volume fraction of packed red blood cells in the whole blood, $F_{RBC} = 0.25$ is the volume fraction of erythrocytes in the total volume of all blood cells, $F_{Hb} = 0.99$ is the volume fraction of hemoglobin in erythrocytes, and oxygen saturation $SO_2 = 0.6$ [99, 108].

TABLE 1.3: Volume fraction of blood C_{blood} and water C_{H_2O} in the dermal layers of human skin.

	Skin layer	C_{blood}	C_{H_2O}
1	Papillary dermis	0.04	0.5
2	Upper blood net dermis	0.3	0.6
3	Reticular dermis	0.04	0.7
4	Deep blood net dermis	0.1	0.7
5	Subcutaneous fat	0.05	0.7

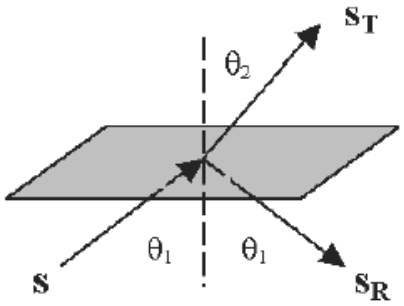

Figure 1.9: Schematic presentation of reflection and refraction of the photon packet at a planar boundary: $\mathbf{s}$ is a direction unit vector of an incident photon packet, $\mathbf{s}_R$ is a direction unit vector of the reflected photon packet, $\mathbf{s}_T$ is a direction unit vector of the transmitted/refracted photon packet.

1.2.5 Reflection and refraction

Fresnel reflection at the surface of an organ can be thought of as a macroscopic scattering, which is *dependent* on the direction of incoming light relative to the tissue surface normal. The refractive indices of a number of tissues have been measured and estimated to be in the range from 1.38 to 1.41 at 633 nm with an approximate decrease of 1% per 100 nm in the visible part of the spectrum [88, 122]. However, subcutaneous tissue is an exception having a refractive index of approximately 1.44.

For light incident at small to intermediate angles on air-tissue and water-tissue interfaces, the refractive indices of this order of magnitude result in Fresnel reflection in the order of about 4% and less than 1%, respectively. However, for small source-detector separations the total effect is considerable.

Therefore, on the media surface, a photon packet undergoes specular reflection and refraction [24], which are taken into account by splitting the photon packet into the reflected and the transmitted parts, the weights of which are attenuated as:

$$W = W_0 (1 - R_{in}) \left[\prod_{p=1}^{M} \Re(\xi) \right] (1 - R_{out}), \tag{1.50}$$

where W_0 is the initial weight of the photon packet, M is the number of the photon packet reflections/refractions at the internal boundary interfaces, including total internal reflection from the outer boundaries, R_{in} and R_{out} account for reflections on the medium/air boundary, when the photon packet enters and leaves the medium respectively. Internal boundaries are treated differently from the surface between the two scattering regions of media. The photon packet is kept as a whole and in an unbiased manner decides if all of the photon packets are either reflected or transmitted. $\Re(\xi)$ is the Fresnel reflection coefficient $\Re(\xi) = R$, when the packet is reflected, which occurs if $\xi \leq R$, or $\Re(\xi) = 1 - R$, if it is transmitted into the medium 2, when $\xi > R$. R is defined as follows (Fig. 1.9):

$$R = \begin{cases} \dfrac{(n_2 - n_1)^2}{(n_2 + n_1)^2} & \text{if } \theta_1 = 0 \\ \dfrac{1}{2} \left[\dfrac{\sin^2(\theta_1 - \theta_2)}{\sin^2(\theta_1 + \theta_2)} + \dfrac{\tan^2(\theta_1 - \theta_2)}{\tan^2(\theta_1 + \theta_2)} \right] & \text{if } 0 < \theta_1 < \theta_{cr} \\ 1 & \text{if } \theta_{cr} \leq \theta_1 < \dfrac{\pi}{2} \end{cases} \tag{1.51}$$

Either reflected or transmitted/refracted, the photon packet changes its direction that is accounted

for by Snell's law [24]. Since the azimuthal angle φ (Figure 1.9) does not change under either reflection or refraction, in terms of the direction cosines transmission/refraction from a medium 1 into a medium 2 is equivalent to

$$\begin{pmatrix} s_1 \\ s_2 \\ s_3 \end{pmatrix}_T = \begin{pmatrix} s_1 \frac{n_1}{n_2} \\ s_2 \frac{n_1}{n_2} \\ \begin{cases} +\sqrt{1-(1-s_3^2)(\frac{n_1}{n_2})^2}, & \text{if } s_3 \geq 0 \\ -\sqrt{1-(1-s_3^2)(\frac{n_1}{n_2})^2}, & \text{if } s_3 < 0 \end{cases} \end{pmatrix}, \tag{1.52}$$

and reflection is equivalent to

$$\begin{pmatrix} s_1 \\ s_2 \\ s_3 \end{pmatrix}_R = \begin{pmatrix} s_1 \\ s_2 \\ -s_3 \end{pmatrix}. \tag{1.53}$$

where $\mathbf{s} = \{s_1, s_2, s_3\}$ is a direction unit vector of an incident photon packet, $\mathbf{s}_T$ is a direction unit vector of transmitted photon packet, $\mathbf{s}_R$ is a direction unit vector of reflected photon packet. Note that angles θ_1 and θ_2 are found from Snell's law: $n_1 \sin\theta_1 = n_2 \sin\theta_2$, where n_1 and n_2 are the refractive indices of the media 1 and 2, respectively. In transition from a medium with a higher refractive index to one with a lower refractive index, total internal reflection occurs for angles larger than the critical angle $\theta_{cr} = \sin^{-1}\frac{n_2}{n_1}$.

Thus, given a photon packet position $\mathbf{r}_i$, its direction $\mathbf{s}_i$ and the proposed path length distance l_i, the distance to the bounding interface is calculated from basic knowledge of geometry. A simple plane interface only is considered in this chapter. However, the same approach can be applied for almost any surface, including rough interfaces; see for example [93, 94].

The general equation for a plane of arbitrary orientation is:

$$\mathbf{n} \cdot (\mathbf{r} - \mathbf{P}_0) = 0, \tag{1.54}$$

where $\mathbf{n}$ is the unit normal to the plane, and $\mathbf{P}_0$ is a radius-vector of any point on the surface of the plane. Inserting (1.28) in (1.54) and solving for l_i gives:

$$l_i^* = -\frac{\mathbf{n} \cdot (\mathbf{r}_i - \mathbf{P}_0)}{\mathbf{n} \cdot \mathbf{s}_i}, \tag{1.55}$$

Thus, instead of the full distance l_i, the packet travels the distance l_i^* to the interface or boundary, where reflection or transmission occurs. Then the distance to the interface is subtracted from the path length $l_i^{**} = l_i - l_i^*$. If the photon packet is reflected, it continues to move with the path length l_i^{**} in the direction given by $\mathbf{s}_R$, (1.53). Otherwise, it is transmitted in the direction given by $\mathbf{s}_T$, (1.52), with the path length l_i^{**} that is scaled following the difference of scattering coefficients, see (1.36).

An example of specular reflection and refraction simulated by MC for a semi-infinite medium with the scattering coefficient $\mu_s = 30\ \text{mm}^{-1}$ and a zero absorption, $g = 0.9$, $n = 1.5$ are presented in Figure 1.10. All photon packets are injected perpendicularly into a homogeneous semi-infinite medium at point $(0,0,0)$. The statistical weight of *singly-refracted* photon packets were collected as a function of the angle of exit, θ_t. Thus, W_1 denotes the weight of refracted photon packets, $W_1 = (1-R_0)(1-R(\theta_i))$, where $\theta_i = \cos^{-1} s_3$. R_0 is the external specular reflection coefficient for light incident normally at the medium/air interface from air. $R(\theta_i)$ is the internal specular reflection coefficient for light incident at the medium/air interface. The excellent agreement is seen between the calculated value of the Fresnel reflectance and the value produced by the MC simulation (see Figure 1.10).

The discrete structure of the MC results is the result of a discrete representation of the Fresnel reflection/refraction coefficients.

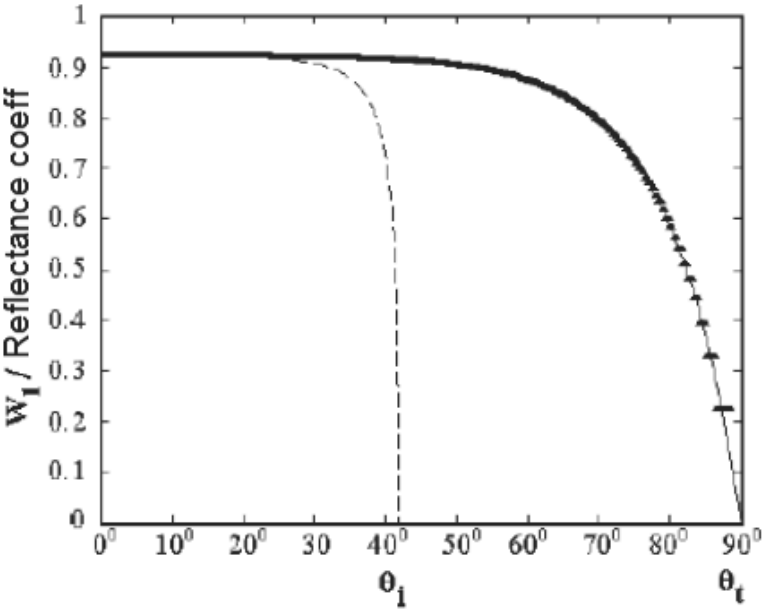

Figure 1.10: Angular distribution of the weight of photon packets emerging from the medium ($n_1 = 1.5$) to another medium ($n_2 = 1.0$). The triangles present the angular distribution of W_1 (MC). The solid and dashed lines are the Fresnel reflectance coefficients $(1-R_0)(1-R(\theta_i))$ as a function of the exit angle θ_t and the angle of incidence θ_i, respectively. Total internal reflection at the critical angle $\theta_{cr} = \sin^{-1}\frac{n_2}{n_1} = 41.8^\circ$ is clearly observed.

The refractive index mismatching at the external boundary results in Fresnel refraction and reflection [123]. To study the effect of mismatching, all the detected photons are grouped into three categories with respect to the number of the photon packet interactions (reflections/refractions) at the outer boundary. The first group, W_1, is a fraction of the detected photon packets that are free of boundary reflections (but may have possible total internal reflections), i.e. these photons have been detected once they crossed the boundary (Figure 1.11). W_2 is a fraction of the detected photons that have been reflected off the boundary once before being detected. The third group, W_3, consists of all the other detected photon packets, i.e. those packets that have reflected off the boundary more than once. The statistical weights of these photon packets are represented by W_1, W_2, and W_3:

$$\begin{aligned} W_1 &= W_0^{'}(1-R(\theta_i)), \\ W_2 &= W_0^{'}(1-R(\theta_i))R(\theta_i), \\ W_3 &= W_0^{'}\sum_{k=3}^{M}(1-R_k(\theta_i))\prod_{j=1}^{k-1}R_j(\theta_i). \end{aligned} \tag{1.56}$$

where $W_0^{'} = W_0(1-R_{in})$ and W_0 is the initial weight of the photon packet, M is the number of the photon packet reflections/refractions at the internal medium interfaces, including total internal reflection from the outer boundaries, and R_{in} accounts for reflection, when the photon packet enters the medium. Note that for W_3 $M \geq 3$ (see Eq. 1.50).

Spatial photon weight distributions W_1, W_2, W_3 versus radius of the detector area (r_D) are demonstrated in Figure 1.12 for a non-absorbing and absorbing media. The discrete structure of the sta-

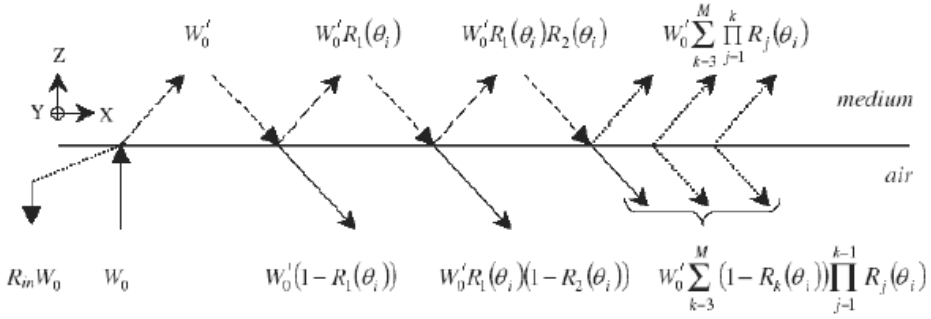

Figure 1.11: Schematic of reflections and refractions of photon packet interactions at the outer boundary of a medium. W_0 is the initial weight of a photon packet, R_{in} is the Fresnel coefficient of the initial specular reflection. $W_0^{'} = (1 - R_{in})W_0$ is the photon packet weight after initial specular reflection. $R(\theta_i)$ is the Fresnel reflection coefficient, and θ_i is the angle of incidence. W_1 is a fraction of the detected photon packets that are free of boundary reflections (except possible total internal reflections), i.e. these photons are detected once they have crossed the boundary. W_2 is a fraction of the detected photons that have been reflected once off the boundary before being detected. W_3 consists of all the other detected photon packets, i.e. those packets that have reflected off the boundary more than once.

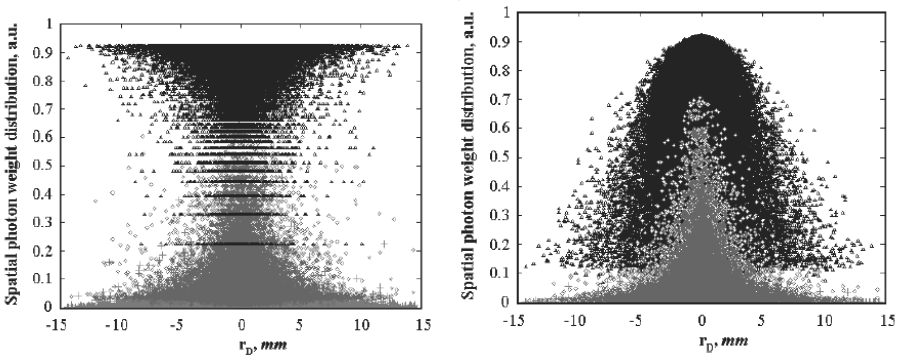

Figure 1.12: Spatial photon weight distribution versus radius of the detector area (r_D): (a) a non-absorbing medium (b) an absorbing medium, $\mu_a = 0.01$ mm^{-1}. The triangles (▲) specify the weight of the photon packets which have experienced one reflection/refraction event on the air-medium boundary, diamonds (◊) represent the weight of the photon packets having acted on the medium boundary twice, crosses (+) show the weight of the high order photon packets reflected/refracted on the air-medium boundary. The optical properties of a semi-infinite highly scattering medium are: $\mu_s = 30$ mm^{-1}, $g = 0.9$, $n = 1.5$.

tistical weight distribution has resulted from a discretization of the Fresnel reflection coefficient, is clearly seen in Figure 1.12 (a), and is completely masked by absorption in Figure 1.12 (b).

Thus, the inclusion of boundaries/interfaces permits the development of applications in complex multi-layered media with inclusions of inhomogeneities. These objects can be very simple, such as a planar interface between two semi-infinite media or a collection of objects such as a complex radiation source or detector. The technique to address both of these problems is essentially the same. The position of a photon packet within the medium is identified by a region number (e.g. number

of layer), its position, its direction towards the boundary, etc. Thus, when the new region number is defined in the MC transport routine, it merely has to check whether or not the optical parameters of the medium have changed and then take appropriate action.

1.3 Monte Carlo Modeling of Coherent Effects

Coherence is one of the fundamental parameters of laser radiation and characterizes the degree to which the oscillating electromagnetic laser radiation maintains a near-constant phase shift in space and time. Despite multiple scattering, coherent effects such as the coherent backscattering (CBS) and spatial and temporal intensity correlations are observed due to the wave nature of light in various dielectric media, such as colloid suspensions, liquid crystals and biological tissues [124–126]. This has triggered active research in the field of optics during the past decades [11, 20, 127–131].

The stochastic MC techniques are widely employed in the studies of coherent effects in multiple scattering randomly inhomogeneous media [127, 129–135].

1.3.1 Field correlation transfer

Let a medium occupy a half space $z > 0$, where z is the Cartesian coordinate normal to the boundary. Field correlation transfer in a randomly inhomogeneous medium with temporal and spatial fluctuations of the dielectric permittivity is described by the integral Bethe-Salpeter equation [19, 136]:

$$\widehat{\Gamma}(\mathbf{R}_2,\mathbf{R}_1,t\,|\,\mathbf{k}_s,\mathbf{k}_i) = k_0^4\widetilde{G}(\mathbf{k}_s-\mathbf{k}_i,t)\delta(\mathbf{R}_2-\mathbf{R}_1)\widehat{I}+ \\ + k_0^4\int d\mathbf{R}_3\widetilde{G}(\mathbf{k}_s-\mathbf{k}_{23},t)\widehat{\Lambda}(\mathbf{R}_2-\mathbf{R}_3)\widehat{\Gamma}(\mathbf{R}_3,\mathbf{R}_1,t\,|\,\mathbf{k}_{23},\mathbf{k}_i), \quad (1.57)$$

where the fourth-rank tensor $\widehat{\Gamma} = \Gamma_{\beta_1\beta_2\alpha_1\alpha_2}(\mathbf{R}_2,\mathbf{R}_1,t\,|\,\mathbf{k}_s,\mathbf{k}_i)$ is the propagator or the Green's function of the Bethe-Salpeter equation. It describes the propagation of two complex-conjugated electromagnetic fields between a point $\mathbf{R}_1$ and a point $\mathbf{R}_2$. Notice that these fields arrive at $\mathbf{R}_2$ delayed by the time t. Vectors $\mathbf{k}_i$ and $\mathbf{k}_s$ are the wave-vectors of incident and scattered plane waves, indices $\alpha_1\alpha_2$ and $\beta_1\beta_2$ being polarization indices of the incident and scattered fields. $|\mathbf{k}_i| = |\mathbf{k}_s| = k = k_0 n$, $k_0 = 2\pi/\lambda$ is the wave-number, λ is the wavelength, and $n = n_1 + in_2$ is the refractive index of the medium. The real part n_1 determines the reflectivity mismatch at the medium boundary. The imaginary part of n determines the photon mean free path length $(2n_2k_0)^{-1} = l$. Vector $\mathbf{k}_{ij} = k(\mathbf{R}_i-\mathbf{R}_j)|\mathbf{R}_i-\mathbf{R}_j|^{-1}$ determines the wave-vector between $\mathbf{R}_i$ and $\mathbf{R}_j$.

The fourth-rank tensor $\widehat{\Lambda}(\mathbf{R})$

$$\Lambda_{\alpha\beta\mu\nu}(\mathbf{R}) = \left(\widehat{I}-\frac{\mathbf{R}\otimes\mathbf{R}}{R^2}\right)_{\alpha\mu}\left(\widehat{I}-\frac{\mathbf{R}\otimes\mathbf{R}}{R^2}\right)_{\beta\nu}\frac{\exp(-R/l)}{R^2} \quad (1.58)$$

is a direct product of the conjugated pair of the Green's functions of Maxwell's equations in a far-field zone. It describes a transformation of a pair of fields with polarization μ and ν into a pair of fields with polarization α and β as a result of a single scattering.

In a weak scattering limit $\lambda \ll l$, which usually fulfills in the dielectric media, $\widetilde{G}(\mathbf{q},t)$ is a Fourier transform of the permittivity correlation function:

$$\widetilde{G}(\mathbf{q},t) = \frac{1}{(4\pi)^2}\int d\mathbf{r}\langle\delta\varepsilon(0,0)\delta\varepsilon(\mathbf{r},t)\rangle\exp(-i\mathbf{q}\mathbf{r}). \quad (1.59)$$

An important statement in the multiple scattering problems, the so-called optical theorem relates the single scattering cross section and the scattering length $l_s = \mu_s^{-1}$. In the Born approximation for electromagnetic field the optical theorem takes the form:

$$l_s^{-1} = \Gamma_R^{-1} k_0^4 \int d\Omega_s \widetilde{G}_0(\mathbf{k}_s - \mathbf{k}_i), \tag{1.60}$$

where $\widetilde{G}_0(\mathbf{k}_s - \mathbf{k}_i)$ is the Fourier transform of the statistical correlator of the dielectric permittivity fluctuations, $\Gamma_R = 2(1 + \overline{\cos^2\theta})^{-1}$ is a Rayleigh factor, $\overline{\cos^2\theta}$ is the square cosine of the scattering angle θ between vectors $\mathbf{k}_i$ and $\mathbf{k}_s$ weighted by the single scattering cross section:

$$\overline{\cos^2\theta} = \frac{\int d\Omega_s \widetilde{G}_0(\mathbf{k}_s - \mathbf{k}_i)\cos^2\theta_s}{\int d\Omega_s \widetilde{G}_0(\mathbf{k}_s - \mathbf{k}_i)}. \tag{1.61}$$

Photon MFP l is given by

$$\frac{1}{l} = \frac{1}{l_s} + \frac{1}{l_a}, \tag{1.62}$$

where l_a is the characteristic length absorption induced by inelastic scattering. For media investigated l_a is much greater than l and, consequently, l/l_s is close to 1.

The normalized correlation function of dielectric permittivity fluctuations is defined as:

$$p(\mathbf{k}_i - \mathbf{k}_s, t) = \frac{\widetilde{G}(\mathbf{k}_i - \mathbf{k}_s, t)}{\int \widetilde{G}(\mathbf{k}_i - \mathbf{k}_s, 0) d\Omega_s}. \tag{1.63}$$

For $t = 0$, $p(\mathbf{k}_i - \mathbf{k}_s, t)$ transforms into the scattering phase function $p_0(\mathbf{k}_i - \mathbf{k}_s) = p(\mathbf{k}_i - \mathbf{k}_s, 0)$, which describes the single scattering cross section.

Iterating the Bethe-Salpeter equation (1.57) and bearing in mind the optical theorem (1.60), one obtains the series of scattering orders

$$\begin{aligned}\widehat{\Gamma}(\mathbf{R}_2, \mathbf{R}_1, t|\mathbf{k}_s, \mathbf{k}_i) = \Gamma_R l_s^{-1} p(\mathbf{k}_i - \mathbf{k}_s, t)\delta(\mathbf{R}_2 - \mathbf{R}_1)\widehat{I} + \Gamma_R^2 l_s^{-2} p(\mathbf{k}_s - \mathbf{k}_{21}, t)\times \\ \widehat{\Lambda}(\mathbf{R}_{21}) p(\mathbf{k}_{21} - \mathbf{k}_i, t) + \Gamma_R^3 l_s^{-3} \int d\mathbf{R}_3 p(\mathbf{k}_s - \mathbf{k}_{23}, t)\widehat{\Lambda}(\mathbf{R}_{23}) p(\mathbf{k}_{23} - \mathbf{k}_{31}, t)\times \\ \widehat{\Lambda}(\mathbf{R}_{31}) p(\mathbf{k}_{31} - \mathbf{k}_i, t) + \ldots,\end{aligned} \tag{1.64}$$

which is usually illustrated by ladder diagrams [137].

In the far-field zone the temporal field correlation function of the scattered radiation can be expressed as the sum of the non-coherent and interference components:

$$\widehat{C}^E(t\,|\,\mathbf{k}_s, \mathbf{k}_i) = \widehat{C}^{(L)}(t\,|\,\mathbf{k}_s, \mathbf{k}_i) + \widehat{C}^{(V)}(t\,|\,\mathbf{k}_s, \mathbf{k}_i), \tag{1.65}$$

where $\widehat{C}^{(L)}(t\,|\,\mathbf{k}_s, \mathbf{k}_i)$ represents the contribution of the ladder diagrams, which describe the non-coherent component, and $\widehat{C}^{(V)}(t\,|\,\mathbf{k}_s, \mathbf{k}_i)$ is the interferential component observed in the backscattering direction.

For normal incidence and almost backscattering direction, ladder and interferential components of the temporal correlation function have the forms [138, 139]:

$$\begin{aligned}C^{(L)}_{\beta_1\beta_2\alpha_1\alpha_2}(t\,|\,\mathbf{k}_s, \mathbf{k}_i) = \int d\mathbf{R}_1 d\mathbf{R}_2 \Gamma_{\beta_1\beta_2\alpha_1\alpha_2}(\mathbf{R}_2, \mathbf{R}_1, t\,|\,\mathbf{k}_s, \mathbf{k}_i)\times \\ \times \exp\left(-\frac{z_1 + z_2}{l}\right),\end{aligned} \tag{1.66}$$

and

$$C^{(V)}_{\beta_1\beta_2\alpha_1\alpha_2}(t\,|\,\mathbf{k}_s,\mathbf{k}_i) = \int d\mathbf{R}_1 d\mathbf{R}_2 \left[\Gamma_{\beta_1\alpha_2\alpha_1\beta_2}\left(\mathbf{R}_2,\mathbf{R}_1,t\,\middle|\,\frac{\mathbf{k}_s-\mathbf{k}_i}{2},\frac{\mathbf{k}_i-\mathbf{k}_s}{2}\right) - \right.$$
$$\left. - k_0^4 \widetilde{G}(\mathbf{k}_s-\mathbf{k}_i,t)\delta(\mathbf{R}_2-\mathbf{R}_1)\delta_{\alpha_1\beta_1}\delta_{\alpha_2\beta_2} \right] \exp\left(-\frac{z_1+z_2}{l} + i(\mathbf{k}_s+\mathbf{k}_i)_\perp \cdot (\mathbf{R}_2-\mathbf{R}_1)_\perp \right), \quad (1.67)$$

where subscript $\perp$ denotes the component perpendicular to the normal to the medium boundary. Clearly, for exact backscattering $\mathbf{k}_s = -\mathbf{k}_i$, the polarized component of the interferential contribution $\widehat{C}^{(V)}(t\,|\,\mathbf{k}_s,\mathbf{k}_i)$ exactly equals the polarized component of the main, non-coherent contribution $\widehat{C}^{(L)}(t\,|\,\mathbf{k}_s,\mathbf{k}_i)$ prior to subtracting the single scattering contribution. Depolarized components are not equal.

The methods using light to study motions by means of speckle fluctuations have appeared with numerous names over the years [140–146]. For particles that are undergoing random relative motion, e.g., Brownian motion, the phases of the individual scattered waves are changing randomly and independently of the other scattered waves. The intensity at the detector will thus fluctuate. The time scale of the intensity fluctuations is related to the rate at which the phase of the scattered waves is changing and thus depends on the motion of the scattering particles and on the momentum transfer $\mathbf{q}$. The intensity fluctuations are more rapid at larger scattering angles and for faster moving particles. The field correlation function is explicitly related to the motions within the sample under study.

The non-coherent component defines the temporal field correlation function:

$$g_1(t) = \frac{C^{(L)}(t\,|\,-\mathbf{k}_i,\mathbf{k}_i)}{C^{(L)}(0\,|\,-\mathbf{k}_i,\mathbf{k}_i)}. \quad (1.68)$$

CBS is an interferential enhancement of the average scattered intensity reflected off a disordered scattering medium [138]. It originates from a two-wave constructive interference near exact backscattering between waves traveling along a given scattering path and its time-reversed counterpart. Physically, it is obvious that the effect will dephase rapidly away from backscattering. For classical scatterers, bearing on general symmetry arguments valid in the absence of any magnetic field, the CBS interfering amplitudes have been shown to have equal weights at exact backscattering in the so-called parallel polarization channels [147]. In the linear-linear channel the incoming and detected light fields have the same linear polarization. In the perpendicular channels, nothing ensures the equality of the two interfering amplitudes, and the contrast of the interference is decreased. Notice that single scattering events require a separate treatment as direct and reversed paths coincide in the backward direction and do not contribute to the CBS enhancement.

The interferential component (1.67) at $t = 0$ describes the CBS intensity peak:

$$I^{CBS}(\theta_s) = \frac{C^{(V)}(0\,|\,\mathbf{k}_s,\mathbf{k}_i)}{C^{(V)}(0\,|\,-\mathbf{k}_i,\mathbf{k}_i)} \quad (1.69)$$

and its angular dependence.

1.3.2 Scalar field

As mentioned above, in the Born approximation the Bethe-Salpeter equation can be represented as a series of scattering orders, which is equivalent to a series of the ladder diagrams. To develop a general stochastic method for coherent effects modeling, a relation will be established between the analytical procedure of the summation of successive terms of a ladder-diagram series and the conventional MC technique.

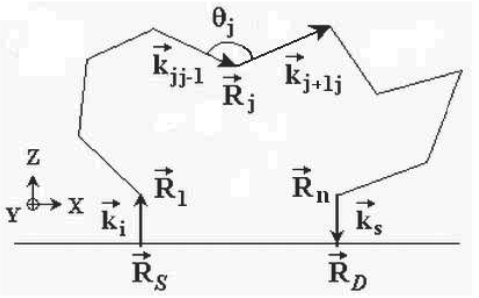

Figure 1.13: Stochastic trajectory of a photon between a point of source $\mathbf{R}_S$ and a point of detector $\mathbf{R}_D$. $\mathbf{R}_1$ and $\mathbf{R}_n$ are the points of the first and final scattering events. Vectors $\mathbf{k}_{jj-1}$ and $\mathbf{k}_{j+1j}$ are wave-vectors before and after the j-th scattering event at $\mathbf{R}_j$, θ_j is the angle between them.

First, let's consider scalar fields. For a scalar field, a tensor $\widehat{\Lambda}(\mathbf{R})$ is transformed into a scalar function $\Lambda_0(R)$=$R^{-2}\exp(-R/l)$, and the Rayleigh factor Γ_R becomes equal to 1. The first term of an iterative series (1.64) describes single scattering, second term – double scattering, etc.

The conventional MC method describes the propagation of optical radiation as a stochastic process, which consists of one, two, ... n scattering events. The difference between iterative solution (1.64) and conventional radiative transfer equation (1.1) is just a matter of how one writes them. Indeed, in terms of numerical simulation, an extra term $\widehat{\Lambda}(R_{jj-1})p_0(\mathbf{k}_j-\mathbf{k}_{j-1})$ in eq. (1.64) is equivalent to simulation of photon transport for a distance $R=|\mathbf{R}_j-\mathbf{R}_{j-1}|$ in a direction $\mathbf{k}_j$. It is very similar to how the conventional MC method works. Indeed, as a results of the MC simulation a stochastic trajectory of a photon appears. It has the origin at a point $\mathbf{R}_0=\mathbf{R}_S$ followed by n sequent points $\mathbf{R}_1$, $\mathbf{R}_2$, $\mathbf{R}_3$,..., $\mathbf{R}_n$, which represents n scattering events, and a point $\mathbf{R}_D$, where the photon packet is detected (Figure 1.13).

The difficulties associated with the iterative solution to the Bethe-Salpeter equation are that the integrals over $\mathbf{R}_i$ cannot be factorized, i.e. integration over particular $\mathbf{R}_i$ cannot be performed independently from the rest or at least some of $\mathbf{R}_i$. In numerical MC modeling a direction and the length of the next photon step are determined in an unbiased way that helps to make this kind of factorization.

Due to the way the phase function is defined, i.e.

$$\int p_0(\mathbf{k}_i-\mathbf{k}_s)d\Omega=1 \tag{1.70}$$

the statistical weight of a photon packet does not change after scattering. In theoretical description, this is granted by the optical theorem. Indeed, $\int\Lambda_0(R)d\mathbf{R}=4\pi l$, hence, the expansion parameter of eq. (1.64) is equal to

$$l_s^{-1}\int d\Omega_n\int d\mathbf{R}_{j+1}\Lambda_0(\mathbf{R}_{j+1}-\mathbf{R}_j)p_0(\mathbf{k}_{j+1}-\mathbf{k}_j)=l_s^{-1}l. \tag{1.71}$$

In the absence of absorption, $l_s^{-1}l$ is exactly equal to 1, that is the evidence of photon weight conservation. Notice that it is the close affinity of the expansion parameter $l_s^{-1}l$ to 1, that brings about all difficulties with the analytical solution of the Bethe-Salpeter equation. That is, the series (1.64) does not converge if the finite number of the terms is involved in consideration.

Calculation of the temporal intensity correlation function with MC is similar to the diffuse reflectance simulation. However, after each scattering event, the direction of a photon packet is determined by a more generalized phase function $p(\mathbf{k}_j-\mathbf{k}_{j-1},t)$, which is dependent on the time delay t.

In most applications such as DWS [143, 144, 148], one studies temporal evolution of inhomogeneities within a medium and considers the Brownian mechanism of temporal decay of inhomogeneity fluctuations. Under these conditions, the temporal permittivity correlation function can be represented as a product of the static correlator $G(q,0)$ and exponential function (see eq. 1.63):

$$p(q,t) \approx p_0(q)\exp(-D_s q^2 t), \tag{1.72}$$

where D_s is a self-diffusion coefficient, and $q = |\mathbf{q}|$ is the wave vector transfer $\mathbf{q} = \mathbf{k}_i - \mathbf{k}_s$, $q = 2k\sin\theta_s/2$.

Thus, to proceed from calculation of the intensity to calculation of the temporal field correlation function one has to replace the phase function according to:

$$p_0(\mathbf{k}_{j-1} - \mathbf{k}_j) \to p_0(\mathbf{k}_{j-1} - \mathbf{k}_j)\exp(-D_s|\mathbf{k}_{j-1} - \mathbf{k}_j|^2 t). \tag{1.73}$$

In the diffusion approximation the momentum transfer is changed to its average:

$$\exp\left(-D_s|\mathbf{k}_{j-1} - \mathbf{k}_j|^2 t\right) \to \exp\left(-2(t/\tau)(1 - \overline{\cos\theta_s})\right) \to \exp\left(-2(t/\tau)(l/l^*)\right), \tag{1.74}$$

where $\tau = (D_s k^2)^{-1}$ is the characteristic time of scattering particle diffusion at distance comparable to the wavelength, $\overline{\cos\theta_s} = g$ is the mean cosine of the scattering angle θ_s, and $l^* = l_s(1-g)^{-1}$ is the transport length.

Thus, in the MC simulation the temporal field correlation function is given by:

$$g_1(t) = \sum_{i=1}^{N_{ph}} W_{di} \exp\left(-2\frac{t}{\tau} n_i \left[1 - \frac{1}{n_i}\sum_{j=1}^{n_i}\cos\theta_j\right]\right), \tag{1.75}$$

where n_i is the number of scattering events experienced by the i-th photon packet, W_{di} is its statistical weight, and θ_j is the scattering angle at the j-th scattering event.

If the interferential component (1.67) is to be modeled then, one notices that the sole difference from the intensity of the non-coherent component (1.66) is a factor $\exp(i\mathbf{k}_\perp\mathbf{R}_\perp)$, where $\mathbf{k}_\perp = (\mathbf{k}_i + \mathbf{k}_s)_\perp$ and $\mathbf{R}_\perp = (\mathbf{R}_1 - \mathbf{R}_2)_\perp$. Due to the translational invariance of $\mathbf{R}_\perp$ in the xy plane, a factor $\exp(i\mathbf{k}_\perp\mathbf{R}_\perp)$ can be substituted with a factor $\cos(\mathbf{k}_\perp\mathbf{R}_\perp)$. Thus, the MC simulation of the CBS intensity can be realized in the following manner. First, one has to exclude the single scattering from the detected signal, as it does not take part in interference. In the case of normal incidence and a small backscattering angle θ_s, the statistical weight of the i-th photon packet, detected at the outer boundary with the wave vector $\mathbf{k}_s$ at the distance $|(\mathbf{R}_S - \mathbf{R}_D^{(i)})_\perp|$ from the source point $\mathbf{R}_S$, is multiplied by a factor $\cos(\mathbf{q}_\perp(\mathbf{R}_S - \mathbf{R}_D^{(i)})_\perp)$. The expression for the CBS intensity is a sum of contributions from all detected photons:

$$I^{CBS}(\theta_s) = \sum_{i=1}^{N_{ph}} W_{di}\cos(\mathbf{k}_\perp(\mathbf{R}_S - \mathbf{R}_D^{(i)})_\perp)(1 - \delta_{n_i,1}), \tag{1.76}$$

where $(1 - \delta_{n_i,1})$ naturally excludes contribution from the singly scattered photons.

The CBS peak or enhancement factor is defined as

$$h^{CBS} = \frac{2I - I_{single}}{I}, \tag{1.77}$$

where I is the non-coherent intensity (1.66) and I_{single} is the intensity of the singly scattered photons.

1.3.3 Polarization

In the case of electromagnetic field, as opposed to scalar field, additional effort has to be made to trace the direction of the electromagnetic field along the photon path that is given by the polarization

vector. According to (1.58) it can be achieved if one calculates the results of n sequential operators applied to the incident field [138]:

$$\prod_{j=1}^{n}\left(\widehat{I}-(\mathbf{R}_{j+1}-\mathbf{R}_j)\otimes(\mathbf{R}_{j+1}-\mathbf{R}_j)|\mathbf{R}_{j+1}-\mathbf{R}_j|^{-2}\right), \tag{1.78}$$

assuming that the photon has experienced n scattering events.

For electromagnetic field, a phase space of a given photon is supplemented with the polarization vector $\mathbf{P}$. In general, $\mathbf{P}$ is a 3-vector and for linear polarization along x axis $\mathbf{P}^{(in)}=(1;0;0)$.

Polarization of the electromagnetic field changes every time after the scattering event. Thus, after each scattering event, when a new direction is determined, a new polarization vector $\mathbf{P}_{j+1}$ is related to $\mathbf{P}_j$ through transformation:

$$\mathbf{P}_{j+1}=\left(\widehat{I}-(\mathbf{R}_{j+1}-\mathbf{R}_j)\otimes(\mathbf{R}_{j+1}-\mathbf{R}_j)|\mathbf{R}_{j+1}-\mathbf{R}_j|^{-2}\right)\mathbf{P}_j. \tag{1.79}$$

Hence, after n scattering events (Fig. 1.13), when a photon packet is detected at a point $\mathbf{R}_D$ the polarization vector is given by:

$$\mathbf{P}^{(out)}=\prod_{j=1}^{n}\left(\widehat{I}-(\mathbf{R}_{j+1}-\mathbf{R}_j)\otimes(\mathbf{R}_{j+1}-\mathbf{R}_j)|\mathbf{R}_{j+1}-\mathbf{R}_j|^{-2}\right)\mathbf{P}^{(in)}. \tag{1.80}$$

If W_{di} is the statistical weight of the detected "scalar" photon, the polarized and depolarized intensities are defined by

$$\begin{aligned} I_{pol}&=I_{XX}=\sum_{i=1}^{N_{ph}}W_{di}P_{ix}^2\Gamma_R^{n_i},\\ I_{depol}&=I_{YX}=\sum_{i=1}^{N_{ph}}W_{di}P_{iy}^2\Gamma_R^{n_i}, \end{aligned} \tag{1.81}$$

where superscript (out) is omitted for brevity. Equations (1.81) describe the non-coherent contribution of ladder diagrams $I_{\beta\alpha}=C^{(L)}_{\beta\beta\alpha\alpha}(0\,|\,\mathbf{k}_s,\mathbf{k}_i)$ (eq. 1.66). Notice that for the exact backscattering direction, the Z component is exactly equal to zero.

In the MC simulation the following expressions are used for polarized and depolarized temporal field correlation functions of the electromagnetic field:

$$\begin{aligned} g^{(1)}_{pol}(t)&=g^{(1)}_{XX}(t)=\sum_{i=1}^{N_{ph}}W_{di}P_{ix}^2\Gamma_R^{n_i}\exp(-2\frac{t}{\tau}n_i(1-\frac{1}{n_i}\sum_{j=1}^{n_i}\cos\theta_j)),\\ g^{(1)}_{depol}(t)&=g^{(1)}_{YX}(t)=\sum_{i=1}^{N_{ph}}W_{di}P_{iy}^2\Gamma_R^{n_i}\exp(-2\frac{t}{\tau}n_i(1-\frac{1}{n_i}\sum_{j=1}^{n_i}\cos\theta_j)), \end{aligned} \tag{1.82}$$

where $P_{i\alpha}$ is the polarization vector of the i-th photon with polarization α. $P_{i\alpha}$ is a result of n_i tensor operators (1.78) applied to the initial polarization, and θ_j is the scattering angle at the j-th scattering event (Fig. 1.13).

1.3.4 Simulation of OCT images

The OCT signal in terms of probing depth z can be presented as an interference term of optical signals coming from the sample and reference arms [149, 150]:

$$I(z)=\left(\langle I_r\rangle\langle I_s\rangle\right)^{1/2}\mathrm{Re}\left\{C(z,l_c)\right\}. \tag{1.83}$$

Here $\langle I_s \rangle$ and $\langle I_r \rangle$ are the mean intensities returning from the sample and reference arms of the interferometer, $C(z, l_c)$ is the normalized coherence function and l_c is the coherence length of probing radiation [151]:

$$l_{\mathrm{c}} = \frac{2\ln 2}{\pi}\frac{\lambda^2}{\Delta\lambda}, \tag{1.84}$$

where $\Delta\lambda$ is the full width at half maximum (FWHM) of the spectrum of source radiation. When performing the MC simulation described above the OCT signal detected at the definite transversal position of the probing beam (A-scan) is calculated for randomly polarized radiation as [152]:

$$I(z) = I_0 \sum_{i=1}^{N_{ph}} \sqrt{W_i} \cos\left(\frac{2\pi}{\lambda}(2z - L_i)\right) \exp\left(-\left(\frac{2z - L_i}{l_{\mathrm{c}}}\right)^2\right), \tag{1.85}$$

where N_{ph} is the number of photons launched, I_0 is a constant defined by instrumental properties of the OCT system, W_i is the weight of i-th detected photon with optical pathlength L_i and $2z$ is the optical pathlength in the reference arm. If one neglects "speckle structure" of the OCT-signal defined by the cosine item, the result can be presented as a superposition of envelopes of partial detected photon contributions [153]:

$$I(z) = I_0 \sum_{i=1}^{N_{ph}} \sqrt{W_i} \exp\left(-\left(\frac{2z - L_i}{l_{\mathrm{c}}}\right)^2\right). \tag{1.86}$$

In order to simulate the 2D OCT image consequent A-scans are simulated with the definite transversal step in probing position. The total number of simulated A-scans and the transversal step between them are predefined regarding the width (FWHM) of the probing beam diameter.

1.3.5 Simulation of polarization dependent OCT signal

Polarization of an electromagnetic wave is typically described in framework of the Stokes-Mueller or Jones formalism [23, 154]. Stokes-Mueller formalism was applied to study polarization in birefringent turbid media for potential application to polarization-sensitive optical imaging [155]. The experimental and numerical studies were carried out to observe the backscattering polarization patterns presented in a form of the Mueller matrices [156, 157]. The residual polarization degree of the backscattered light and its connection to the optical properties of the scattering medium was studied in [158]. To explore the possibility of retrieving the birefringence properties of layered tissue with the depth-resolved polarization-sensitive OCT (PS-OCT) Jones formalism was implemented to reduce long calculation time, typically required in the full Stokes-Mueller approach [159].

Schmitt et al. proposed a method for discriminating short and long path photons that is based on the relationship between the polarization states of incident and forward scattered light [160]. Discussing coherent backscattering and its dependence on the state of polarization of an incident linearly polarized light, Akkermans et al. assumed that for both states of polarization the corresponding intensity can be represented as a product of the intensity of a scalar wave, which does not depend on the polarization state, and a corresponding multiplicative factor (weighting function) describing polarization transfer [138]. These factors are specific for a given polarization state and generally depend on the properties of scattering particles, e.g. size, shape [161, 162]. The expression for the co- and cross-polarized intensities derived from the expression proposed in [162] has been successfully used in [163], whereas the experimental results [164] proved the adequacy of the Akkermans' conjecture of time scales involved in the depolarization process of the backscattered light. Consider a plane electromagnetic wave polarized in the x direction that enters the medium along positive direction of z axis normal to the interface. By a co-polarized wave we understand a linearly polarized scattered wave with the same orientation of polarization as the incident wave,

and a cross-polarized wave is perpendicular to the incident wave direction of polarization [154]. Thus, waves scattered in xz and yz planes define co-polarized and cross-polarized components of the scattered electromagnetic wave, respectively.

To account for the depolarization effect in PS-OCT images we adopted the polarization vector formalism where the polarization is described in terms of a polarization vector $\vec{P}$ undergoing a sequence of transformations after each scattering event [154]. The trajectories of the polarized photons are weighted in accordance with their polarization state. Within the far-field or Fraunhofer approximation the polarization vector of the scattered wave $\vec{P}_{i-1}$ is transformed upon the i-th scattering event into $\vec{P}_i$ as [14, 138]:

$$\vec{P}_i = -\vec{e}_i \times [\vec{e}_i \times \vec{P}_{i-1}] = [\hat{I} - \vec{e}_i \otimes \vec{e}_i]\vec{P}_{i-1}, \tag{1.87}$$

where $\vec{e}_i$ is the unit vector along the propagation direction between $(i-1)$-th and i–th scattering events. Note that although the expression is rigorously introduced for the case of pure Rayleigh scattering, it can also be applied as the first approximation in case of Rayleigh-Gans-Debye (RGD) scattering valid for soft scattering particles with the size comparable to or a few times larger than the wavelength [14]. Namely, the size D of the particles should obey the relation $(\varepsilon_r - 1)D/\lambda \gg 1$ where $(\varepsilon_r - 1)$ is the relative fluctuation of dielectric permittivity between the scatterer (e.g., cell component such as nucleus or mitochondria) and the surrounding medium (e.g., cytoplasm). Typically in biotissues the value of $(\varepsilon_r - 1)$ is less than 0.1 [90] therefore RGD approximation is quite reasonable for the particles with the sizes of units of λ which are characterized by non-isotropic scattering phase function. At the same time, implementation for strongly scattering large inclusions may lead to some discrepancy in the final results; however, this approximation can be applied to qualitatively estimate the effects of depolarization in OCT images. Explicitly, the tensor $\mathbf{S}_i = [\hat{I} - \vec{e}_i \otimes \vec{e}_i]$ is presented as

$$S_i = \begin{pmatrix} 1 - e_{iX}^2 & -e_{iX}e_{iY} & -e_{iX}e_{iZ} \\ -e_{iX}e_{iY} & 1 - e_{iY}^2 & -e_{iY}e_{iZ} \\ -e_{iX}e_{iZ} & e_{iX}e_{iZ} & 1 - e_{iZ}^2 \end{pmatrix}. \tag{1.88}$$

It guarantees that the electromagnetic field remains transversal experiencing the i-th scattering event. The chain $\mathbf{T}(n) = S_n S_{n-1} ... S_1$ of projection operators $\mathbf{S}_i$ transforms the initial polarization upon a sequence of n scattering events to the final polarization:

$$\vec{P}_n = S_n S_{n-1} ... S_1 \vec{P}_0. \tag{1.89}$$

Consequently, propagation of co-polarized and cross-polarized components of the electromagnetic field in the medium is described along the same trajectories obtained for the scalar field. The vector nature of electromagnetic field can be taken into account by multiplying the statistical weight of each trajectory by the square of the matrix element of tensor $\mathbf{T}(n)$: $T_{xx}(n)$ for co-polarized component and $T_{yx}(n)$ for cross-polarized one.

In order to link vector and scalar approaches in simulation of PS-OCT images it should be pointed out that in accordance with the optical theorem [165] the scalar approach yields [136, 161]:

$$k_0^4 \int G(k_i - k_s) d\Omega_s = \frac{1}{s}, \tag{1.90}$$

whereas for the electromagnetic field [136, 163]:

$$k_0^4 \int G(k_i - k_s) d\Omega_s = \frac{2}{1 + \cos^2\theta} \frac{1}{s}. \tag{1.91}$$

Therefore, at every scattering event the multiplicative factor should be included:

$$\Gamma = \frac{2}{1+\cos^2\theta} \tag{1.92}$$

Finally, for linearly polarized probing radiation the expression (1.86) can be re-written separately for co- and cross-polarized detected OCT signal:

$$I_{co}(z) = I_0 \sum_{i=1}^{N_{ph}} \sqrt{W_i \Gamma^{n_i} T_{xx}(n_i)^2} \exp\left(-\left(\frac{2z-L_i}{l_c}\right)^2\right) \tag{1.93}$$

for co-polarized component and

$$I_{cross}(z) = I_0 \sum_{i=1}^{N_{ph}} \sqrt{W_i \Gamma^{n_i} T_{yx}(n_i)^2} \exp\left(-\left(\frac{2z-L_i}{l_c}\right)^2\right) \tag{1.94}$$

for cross-polarized one, where n_i is the number of scattering events for i-th detected photon.

1.3.6 Termination

In order to keep the simulation time within reasonable bounds, a test based on prerequisite cut-off criterion is performed after each photon interaction. If the statistical weight W of the packet is less than a minimal value, typically $W_{min} = 0.0001$ or if the total number of scattering events exceeds the maximum value $N_{max\ scat} = 10000$ it is assumed that the packet no longer significantly contributes to the detected signal and can be terminated. After a number of photon packets has been traced in the medium (typically 10^9–10^{11}), the parameters of interest are scored from the accumulated photon histories.

1.4 Online Object Oriented Monte Carlo Computational Tool for the Needs of Biomedical Optics

As one can see, due to a number of practical OD applications the MC model undergoes continuous modifications and changes dedicated to inclusion of diverse properties of incident optical/laser radiation, configuration of the sources and detectors, structure of the medium and the conditions of light detection [99, 104, 108, 135, 137, 152, 153, 165–174]. Past attempts to unify these MC codes are mainly based on the use of structured programming [175]. While structured programming has been known for years, it limits the ability to handle a large code without decreasing its functionality and manageability [176]. In practice, the increasing diversity of the MC applications results in a substantial growth of the model's source code and leads to the development of a set of separate MC codes each dedicated to a particular purpose.

1.4.1 Object oriented concept of Monte Carlo modeling

To generalize, unify and implement MC modeling for a multi-purpose use in various biomedical optics applications we apply the Object Oriented Programming (OOP) concept [177, 178]. The OOP is widely used in mainstream application development and has been found extremely effective in design of complex multi-parametric systems, providing a highly intuitive approach of programming [176, 179]. The key features of OOP allow the MC to be separated into logical components, described by objects.

Thus, each photon packet has been defined as an object interacting with medium or medium components also defined as objects. Splitting the medium into the objects allows developing the tissue model more iteratively and uniformly. The distribution of scattering centers, macro-inhomogeneities, such as blood vessels, tumors, aneurisms, etc. can be formed by combination of 3D elementary volumes (objects) presenting spatial variations in the tissues. Moreover, actual structure of a biological tissue can be imported into the model as an object (image) provided by OCT, Photo-Acoustic Tomography (PAT), ultrasound, MRI, etc.

Utilizing the inheritance feature of OOP the smart hierarchy structure of the code has been created to prevent creation of multiple classes for similar tasks. The hierarchy allows "allied" objects to share variables and members, significantly reducing the amount of source code and paving the way to extend and generalize the MC for various OD applications. In addition, the variations of scattering phase functions, such as Mie, Rayleigh and Henyey-Greenstein [171] have been defined using the polymorphism feature of OOP that allows one to handle the modeling with no changes of the source code.

Thus, the OOP approach significantly increases the efficiency of the model manageability and provides superior opportunities to generalize MC to combine previously developed MC models as a way to imitate a particular OD experiment taking into account various features of optical radiation and light-tissue interaction. Schematically the structure of the generalized MC approach is shown in Figure 1.14.

As one can see, first, by the selection of a certain application the parameters of the Source, Detector and Scattering medium are entered. Depending on the application, the objects are tuned to the appropriate feature of light-tissue interaction and the simulation is performed. By completing, the output data are prepared in the format utilized in the corresponding OD experiment/application. The OOP MC version supports the estimation of sampling volume offered by a reflectance and/or transmittance geometry (e.g. for fiber optic probe with a small mm source-detector spacing); simulation of reflectance or transmittance optical/near-infrared spectra of the multi-layered media like human skin; modeling of skin color depending on volume fraction of melanin and blood, blood oxygen saturation; modeling of OCT images with regards coherence and polarization properties of probing light, imitation of spatial localization of skin tissue fluorescence excitation and simulation of coherent effects of multiple scattering.

1.4.2 Graphics Processing Unit acceleration of the Monte Carlo model

Launching of a large number of photon packets (typically 10^9-10^{11}) and computing their interaction with the medium and with the probe is a highly intensive computational process. Due to the task intensity, processing time is always a significant issue in stochastic modeling, taking a few days to complete at the standard CPU. To achieve supreme performance of simulation a number of programming approaches and optimizations of algorithms have been used in the past, including parallel and cluster computing [180, 181]. The recently developed parallel computing framework, known as Compute Unified Device Architecture (CUDA), introduced by NVIDEA Corporation has been applied. NVIDEA CUDA technology provides an unlimited access to computational resources of the graphic card: processor cores, different types of memory (of various capacity and speed) making the Graphics Processing Unit (GPU) a massive co-processor in parallel computations [180, 181].

We utilize the recent, introduced in 2010, CUDA generation, so-called architecture codename Fermi. Designed for C/C++ development and easily integrated with the Microsoft Visual Studio it makes parallel programming significantly easier, especially in terms of project management and debugging. The latest CUDA generation supports most of the OOP features like creating classes, inheritance, and polymorphism and keeps all dramatic performance gains of the CUDA computing [177]. The OOP MC model has been developed using CUDA 4.1 C/C++ and supports multiple GPUs, providing user's interface and delivering the modeling output. The hardware is presented by two Tesla M2090 / GeForce GTX 480 graphic cards with NVIDIA CUDA computing capability

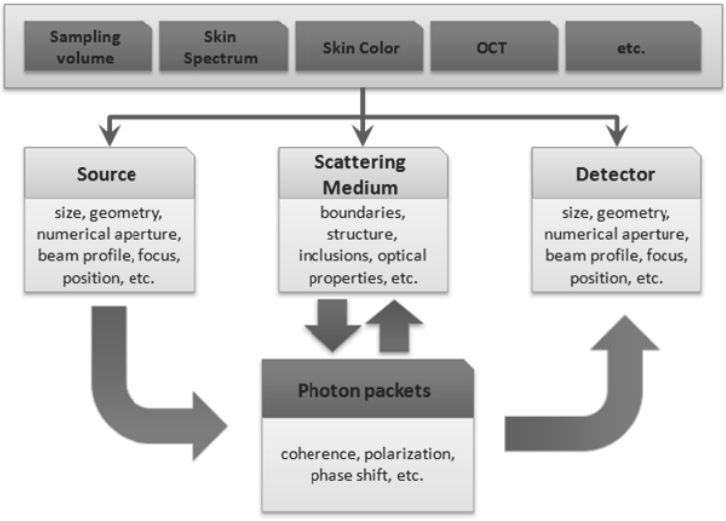

Figure 1.14: Schematic presentation of the generalized object-oriented MC model structure. Data Input and selection of a particular application; Class objects represent exact experimental conditions including source-detector geometry and configuration, medium structure, properties of incident radiation, etc.

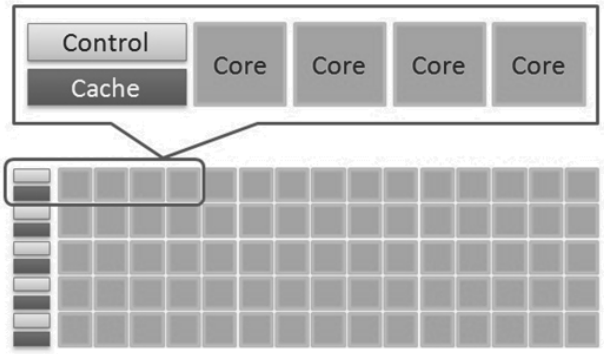

Figure 1.15: Schematic presentation of used GPU logically divided into hundreds of independent cores allowing creation of thousands of lightweight parallel threads.

2.0 having up to 6.0 Tflops of computational power on board (single precision). The graphic chip is logically divided into hundreds of CUDA cores (in our case up to 500 per card), schematically presented in Figure 1.15. Therefore, it executes up to twenty thousand threads simultaneously, without context switch performance losses and very fast (up to 4 Gbit/s) on-chip GDDR memory. The graphic chip's shared memory has been used to store the intermediate results; constant memory is applied for data input, whereas the global memory is used to store parameters of photon objects (e.g. path-length, state of polarization, outlet angles etc.). The tiling and cutoff techniques are used to process large datasets and avoid memory bandwidth limitations [180, 181]. Such a design allows simulating propagation of thousands (15 to 20 depending on application and detector parameters) of photon objects in the medium simultaneously that provides an opportunity for direct imitation of image or wave front transfer in the scattering medium or OCT image modeling.

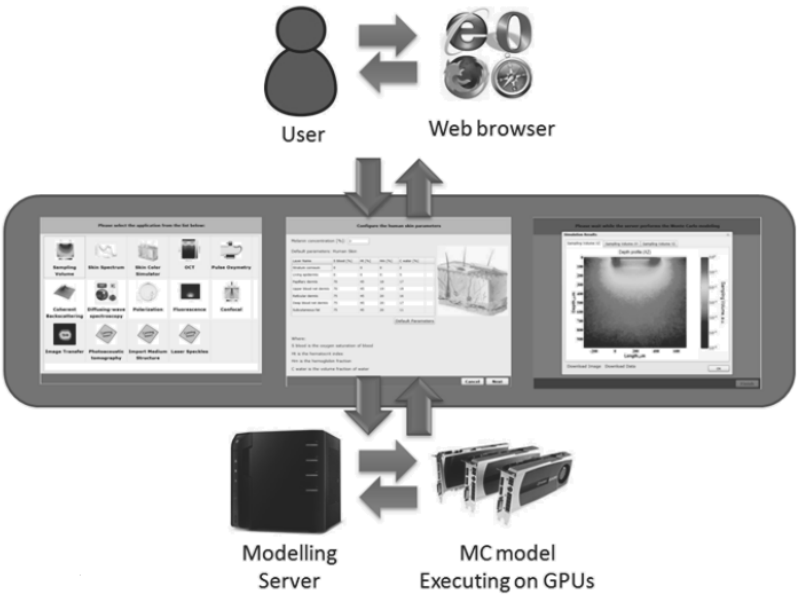

Figure 1.16: Schematic presentation of the key components of the online MC solution. The server hosts a web front end, which accepts user simulation requests and retrieves results. The developed components provide interoperability between the interactive user interface and GPUs.

Specially designed for 3D graphic applications mainly for computer games and professional software designing this cutting edge graphic technology also incorporates a powerful set of instruments applied for optimized simulation of object motion, rotation, reflection, ray-tracing, etc. The NVIDEA CUDA provides GPU-accelerated mathematical libraries, such as CULA, CUBLAS - Linear Algebra, CUFFT - Fast Furrier Transform, CURAND - Random Number Generators [182]. Their incorporation into MC allows speeding up the simulation of each photon packet up to 1000 times.

1.4.3 Online solution and web integration

A flow chart of the online solution is schematically presented on Figure 1.16.

The MC modeling server provides major hardware acceleration by CUDA supporting GPUs. The developed server software consists of the web front end, management part, GPU-web integration and the CUDA-based MC core described above.

The front end of the MC is developed by using Microsoft ASP.NET and Microsoft Silverlight technologies [183–186]. Microsoft Silverlight is used for creation of a cross-platform lightweight interactive interface to access a particular MC application [186], whereas ASP.NET is employed to meet modern design and security requirements [185].

The management part of the MC modeling server consists of the Input / Output (I/O) and Load Balancing systems. The I/O is created to accept and validate user credentials and online input of modeling parameters; to log and store computation enquiries and output data into a server database; to deliver the results of the simulation back to the front end. The I/O works in tandem with the Load Balancing which allows one to manage the server load, monitor running simulations and check the GPU availability. To make the online MC less vulnerable to common network threats and overloads, the management part has been developed utilizing recently added .NET 4.0 features, such as Windows Presentation Foundation (WPF) and Windows Communication Foundation (WCF)

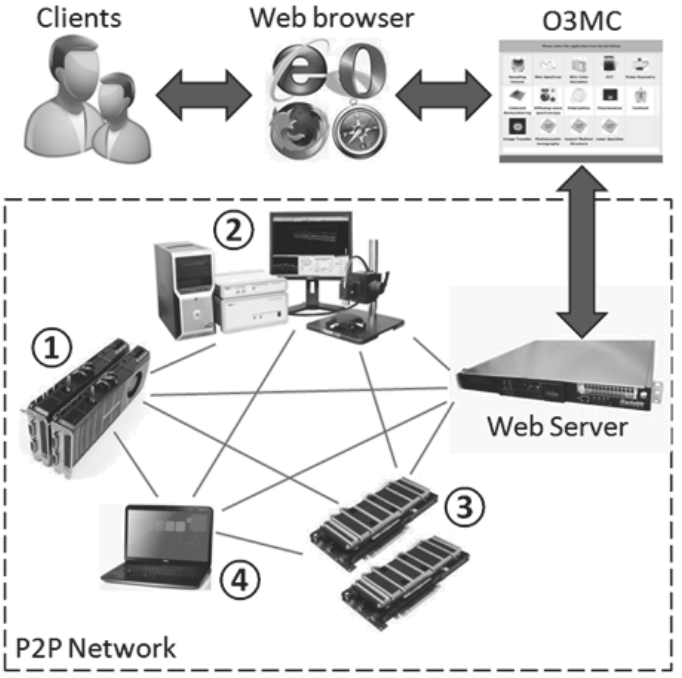

Figure 1.17: Schematic presentation of P2P O3MC implementation. Clients interact with the O3MC web interface via a preferred web browser. The server accepts O3MC simulation requests and keeps track of the participating peers. The P2P network consists of different computers equipped with the CUDA-supporting GPUs: (1) a workstation with two GeForce GTX 480 GPUs each 480 CUDA cores, 1540 Gigaflops of the peak single precision FPP / 85 Gigaflops double precision FPP, 1536 GB of GDDR5 memory; (2) Thorlabs OCT imaging system workstation with Quadro FX580 featuring 32 CUDA cores, 512 MB GDDR3 memory; (3) computational server equipped with two Tesla M2090 GPUs each 512 CUDA cores, 1331 Gigaflops of the peak single precision floating point performance (FPP) / 665 Gigaflops double precision FPP, 6 GB of GDDR5 memory; (4) Dell laptop with GeForce GT555M featuring 144 CUDA cores, 3072 GB GDDR3 memory. Images are adopted from manufacturer websites and/or have a free license.

[187, 188].

It should be pointed out that .NET solutions are executed in the Common Language Runtime (CLR), the core of .NET [184]. Known as a safe managed programming environment the CLR has no direct access to GPUs and other hardware resources. Therefore, to provide the interoperability between the web front end and graphic cards the GPU-web integration component has been developed. The Component Object Model (COM) [189] and .NET interoperability have been used to provide interaction between the binaries produced by C sharp and CUDA compilers. The proposed solution allows multiple users to access GPU computational resources online within a reasonable time (in a range from a few seconds to several minutes). The developed Online Object Oriented MC (O3MC) computational tool is now available at www.biophotonics.ac.nz, and can be used for various applications in biomedical optics as well as in biophotonics and optical engineering [177].

1.4.4 Peer-to-Peer computing infrastructure for the Monte Carlo modeling tool

OOP and GPU implementations enable one to significantly speed up the MC simulation. However, due to the multi-user architecture of the online solution, concurrent simulations by multiple clients could degrade performance of O3MC. For example, if one user accessing the O3MC can get the results in 4.3 seconds on TESLA M2090 GPU, 100 users accessing O3MC at the same time can be stacked in a queue and wait for 10-15 minutes. Therefore, in framework of further development of a tool (available online at: www.biophotonics.ac.nz) to deal with the multi-user access we apply a peer-to-peer (P2P) network. A typical P2P network consists of a set of computers, called nodes or peers, which communicate and share their GPUs (Figure 1.17). The peers in a P2P network are equal among each other, acting both as clients and servers [190]. This approach has gained a lot of popularity in recent years, especially in terms of multimedia content delivery and communication (e.g. BitTorrent, Skype, etc.). With current development we, for the first time to our knowledge, apply a hybrid P2P network (Figure 1.17) utilizing different types of peers for MC simulation.

The web server hosts the online MC tool user interface, accepts O3MC simulation requests from clients and keeps track of the other nodes (Figure 1.17). The nodes are responsible for sharing the information about currently queuing MC simulations, processing them on GPUs, uploading, downloading and hosting the outcomes (presented in a typical journal-paper format) among themselves without the need of the central server. To develop the P2P Network (Figure 1.17) the recently introduced P2P features of .NET 4.0 Windows Communication Foundation (WCF) [191] were applied. This allows integrating the P2P Network with the Load Balancing part of O3MC as both are written in managed code using .NET Framework APIs [177]. Thus, a number of MC simulations can be executed simultaneously on peers without queuing. A specially developed load balancing procedure manages the number of running applications and their distribution on peers/GPUs. Further development of such a network worldwide could be a base for a computational platform for biomedical optics and optical diagnostic community.

1.5 Results of Monte Carlo Simulation

1.5.1 Validation of the technique

To validate the MC model, presented in this chapter, the results of simulations were compared to the predictions of the time-independent diffusion equation for a semi-infinite medium, given by (1.24).

The results of the spatially resolved diffuse reflectance obtained by the MC model directly agree with the results of the steady-state diffusion equation. Figure 1.18 presents a spatially resolved reflectance $R(\rho)$ plotted as a function of the radial distance ρ, where $R(\rho) = \int_0^\infty R(\rho,t)dt$ (see (1.24)). In order to provide better visualization, the simulation was also carried out for the index-matched and index-mismatched medium boundary and the results are presented in terms of natural logarithm of the reflectance multiplied by the square of the radial distance $\ln\left[\rho^2 R(\rho)\right]$ (see Fig. 1.18 b).

Values of R_ϕ, R_j, R_{eff}, C_ϕ, and C_j for typical mismatches of refractive index on the medium boundary are presented in Table 1.4.

Figure 1.19 (a) shows the comparison of time-resolved diffuse reflectance calculated by the diffusion theory, $R(t) = \int_0^\infty R(\rho,t)2\pi\rho d\rho$. Figure 1.19 (b) presents the time dependence of reflectance for a given source-detector separation $\rho = 5$ mm, $R(\rho,t)$, is calculated from the diffusion equation (1.24) and is compared against the results of the MC simulation for a semi-infinite medium with the optical parameters: $\mu_s' = 0.5\ \text{mm}^{-1}$, $\mu_a = 0.02\ \text{mm}^{-1}$, $g = 0.92$, $n = 1$.

Good agreement is obtained in all ranges of time. At least 10 scattering events are required

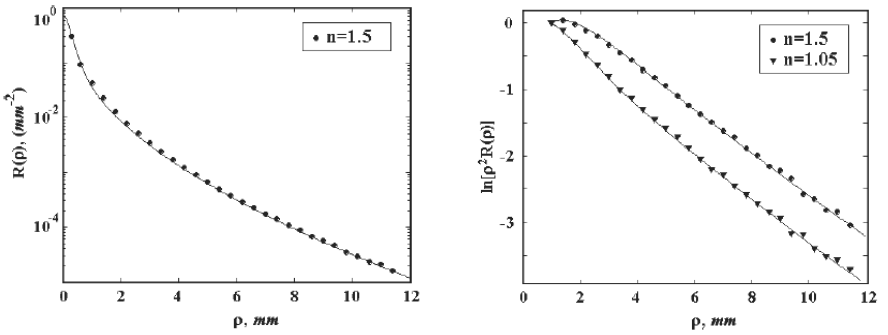

(a) (b)

Figure 1.18: Comparison of the results from MC simulation and the diffusion theory for spatially resolved reflectance from index-mismatched interface of semi-infinite medium: (a) spatially resolved diffuse reflectance $R(\rho)$, (b) a natural logarithm of the reflectance multiplied by the square of the radial distance ρ, $\ln\left[\rho^2 R(\rho)\right]$. The symbols show the results of the MC simulation, and the solid lines are the results of the diffusion theory prediction. The optical parameters are: $\mu_s = 30$ mm^{-1}, $\mu_a = 0.01$ mm^{-1}, $g = 0.9$, $n = 1.5$ (•), and $n = 1.05$ (▼).

TABLE 1.4: $R_\phi, R_j, R_{eff}, C_\phi$, and C_j for the refractive index n of a medium, air ($n_{air} = 1$).

n	R_ϕ	R_j	R_{eff}	C_ϕ	C_j
1	0	0	0	0.25	0.5
1.05	0.1056	0.0355	0.0731	0.2236	0.4822
1.37	0.5057	0.3636	0.4679	0.1236	0.3182
1.4	0.529	0.3888	0.4935	0.1178	0.3056
1.45	0.5645	0.4281	0.5326	0.1089	0.2859
1.5	0.5964	0.4644	0.5678	0.1009	0.2678
1.55	0.625	0.4979	0.5996	0.0937	0.251

to occur before a photon can be qualified as a diffuse photon. Indeed, after 75 *ps* a photon has traveled approximately 23 mm, that for a medium of $\mu_s' = 0.5$ mm^{-1} is equivalent to approximately 10 scattering events.

The results of MC modeling are also well agreed with the theoretical predictions for diffuse reflectance and transmittance performed for an isotropic scattering slab [195]. The solution to the diffusion equation for a finite slab was taken from [195], originally derived by [13]. Albedo $a = \frac{\mu_s}{\mu_s+\mu_a}$ was taken 0.9976, and two different optical thicknesses $\tau = 10$, 20, have been considered, where $\tau = (\mu_s + \mu_a)d$ and d is thickness of a slab (Figure 1.20).

Table 1.5 shows the values for transmittance and reflectance obtained by the MC model in comparison with data tabulated by van der Hulst [192], the results of the adding-doubling method [194, 196], and the MC programs developed by van der Zee [193] and Wang et al. [69] for relative refractive index of 1, a set of four values for albedo a, and four values of a slab thickness for each albedo, respectively.

Van der Hulst [192] obtained the values for the diffuse reflectance and transmittance, for a slab illuminated with a collimated light source normally incident on the medium surface, by the doubling method, which is a representative of an adding-doubling methods family. This was done for the case

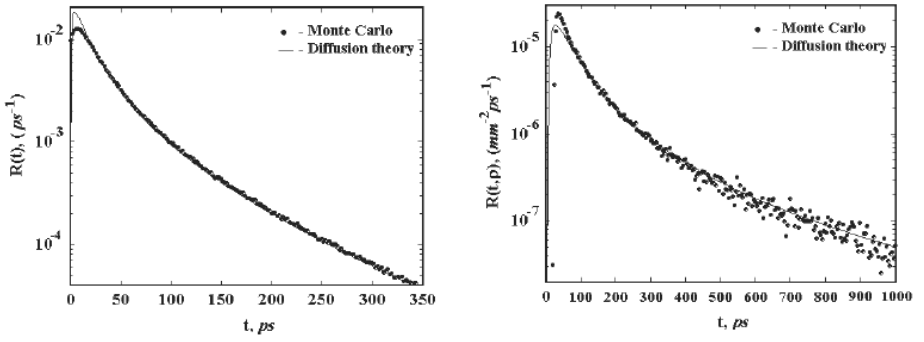

(a) (b)

Figure 1.19: Comparison of the time-resolved results of the MC simulation with that of the diffusion equation: (a) time resolved reflectance $R(t)$, (b) time dependence at a source-detector separation $\rho = 5$ mm, $R(\rho,t)$.

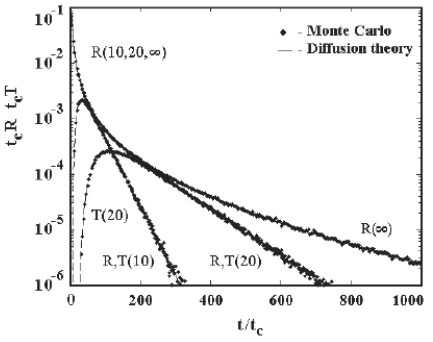

Figure 1.20: Time resolved reflectance and transmittance from an isotropic scattering slab with a plane wave pulse irradiation. Symbols are the MC results, lines are diffusion theory predictions. $R(10,20,\infty)$ and $T(10,20)$ are reflectance and transmittance for $\tau = 10$, 20, and ∞. $t_c = c^{-1}(\mu_s + \mu_a)^{-1}$.

of isotropic and anisotropic scattering, where the HG scattering phase function is used. The values are tabulated as a function of optical depth $\tau = (\mu_s + \mu_a)d$, and albedo $a = \frac{\mu_s}{\mu_s+\mu_a}$ as a parameter, where d is the slab thickness. In all calculations ten MC simulations of 10^6 photon packets each were completed to compute the average and the standard error of the total diffuse reflectance.

In Table 1.6 results are presented for the HG scattering phase function with g values of 0.5, 0.875, and for albedo $a = 0.9$, 0.99. Good agreement can be seen for all these different cases. All digits in the results are meaningful, however, the results of the van der Zee MC code are given with a varying number of accurate digits since no better data have been available to the authors.

The verification of the total diffuse reflectance was carried out for a semi-infinite scattering medium. The average and the standard error of the total diffuse reflectance were computed and compared in the table below with prediction of analytical results of [197], results of the adding-doubling method of [194], and that of the MC code (MCML) developed by [69] versus the developed MC. The medium has the following optical parameters: $\mu_s = 9$ mm^{-1}, $\mu_a = 1$ mm^{-1}, $g = 0.0$ (isotropic scattering), $n = 1.5$. The results are presented in Table 1.7.

TABLE 1.5: Comparison of MC reflectance and transmittance simulations for an isotropic scattering slab with the data tabulated by van der Hulst [192](vdH), van der Zee [193] (vdZ) and Prahl [194] (P).

Optical depth	Reflectance				Transmittance			
τ	MC	vdH	vdZ	P	MC	vdH	vdZ	P
$a = 0.4$								
0.25	0.0356	0.0357	0.037	0.0356	0.8137	0.8136	0.812	0.8136
0.5	0.0554	0.0553	0.0524	0.0553	0.6576	0.6577	0.661	0.6577
1	0.0732	0.0734	0.0716	0.0734	0.4252	0.4250	0.426	0.4251
4	0.0832	0.0833	0.0837	0.0833	0.0272	0.0272	0.0272	0.0272
$a = 0.8$								
0.25	0.0824	0.0824	0.0837	0.0824	0.8594	0.8594	0.858	0.8595
0.5	0.1402	0.1401	0.143	0.1401	0.7377	0.7378	0.734	0.7378
1	0.2108	0.2109	0.209	0.2108	0.5414	0.5414	0.544	0.5414
4	0.2842	0.2840	0.287	0.2840	0.0750	0.0751	0.0754	0.0751
$a = 0.9$								
0.25	0.0965	0.0965	0.0975	0.0965	0.8733	0.8733	0.873	0.8733
0.5	0.1690	0.1690	0.165	0.1690	0.7655	0.7653	0.771	0.7654
1	0.2676	0.2674	0.266	0.2674	0.5915	0.5916	0.594	0.5916
4	0.4082	0.4081	0.408	0.4081	0.1286	0.1285	0.126	0.1285
$a = 0.99$								
0.25	0.1101	0.1101	0.109	0.1101	0.8868	0.8867	0.886	0.8867
0.5	0.1991	0.1989	0.203	0.1989	0.7939	0.7940	0.790	0.7941
1	0.3331	0.3329	0.329	0.3329	0.6508	0.6509	0.655	0.6510
4	0.6452	0.6450	0.645	0.6450	0.2754	0.2755	0.276	0.2755

TABLE 1.6: Comparison of MC reflectance and transmittance simulations for an anisotropic scattering slab, $g = 0.5$ and $g = 0.875$ with the data tabulated by van der Hulst [192] (vdH), van der Zee [193] (vdZ) and Prahl [194] (P).

optical depth	Reflectance				Transmittance			
τ	MC	vdH	vdZ	P	MC	vdH	vdZ	P
$a = 0.9$				$g = 0.5$				
0.5	0.0720	0.0720	0.0739	0.0720	0.8672	0.8672	0.865	0.8672
1	0.1299	0.1298	0.129	0.1298	0.7390	0.7391	0.739	0.7391
4	0.2612	0.2612	0.262	0.2612	0.2505	0.2505	0.249	0.2505
$a = 0.99$				$g = 0.5$				
0.5	0.0879	0.0879	0.0874	0.0878	0.9057	0.9057	0.906	0.9057
1	0.1706	0.1707	0.169	0.1707	0.8147	0.8145	0.816	0.8145
4	0.4700	0.4698	0.467	0.4698	0.4524	0.4527	0.455	0.4527
$a = 0.9$				$g = 0.875$				
0.5	0.0125	0.0125	0.0110	0.0125	0.9354	0.9354	0.935	0.9354
1	0.0238	0.0238	0.0226	0.0238	0.8702	0.8701	0.869	0.8702
4	0.0658	0.0657	0.0650	0.0658	0.5212	0.5212	0.522	0.5212
$a = 0.99$				$g = 0.875$				
0.5	0.0157	0.0157	0.0155	0.0157	0.9789	0.9789	0.979	0.9790
1	0.0327	0.0327	0.0322	0.0327	0.9558	0.9558	0.956	0.9558
4	0.1416	0.1417	0.140	0.1417	0.8003	0.8001	0.802	0.8002

TABLE 1.7: Comparison of the total diffuse reflectance given by analytical results [197], results of the adding-doubling method [194], and MCML [69] versus the developed O3MC [177].

Source	R_d	*error*
Giovanelli [197]	0.2600	–
MCML [69]	0.25907	0.00170
Adding-doubling [194]	0.26079	0.00079
O3MC [177]	0.25957	0.00043

TABLE 1.8: Comparison of the total diffuse reflectance and transmittance given by tabulated data [192], results of the adding-doubling method [194], and MCML [69] versus the developed O3MC [177].

Source	R_d	*error*	T_d	*error*
Van der Hulst [192]	0.09739	–	0.66096	–
MCML [69]	0.09734	0.00035	0.66096	0.00020
Adding-doubling [194]	0.09711	0.00033	0.66159	0.00049
O3MC [177]	0.09741	0.00027	0.66096	0.00017

The columns R_d and *error* are the average and the standard error of the total diffuse reflectance. The average values and error were computed similarly after ten MC simulations of 50000 photon packets each. The medium has the following optical parameters: $\mu_s = 9$ mm^{-1}, $\mu_a = 1$ mm^{-1}, $g = 0.75$ (anisotropic scattering), $n = 1$, and slab thickness $d = 0.2$ mm.

1.5.2 Comparison with the human skin diffuse reflectance spectrum and color measured *in vivo*

Skin diffuse reflectance spectra was simulated by the MC technique assuming a wavelength-independent scattering coefficient for the different skin tissues and using the known wavelength dependence of the absorption coefficients of main skin tissue absorbers, such as oxy- and deoxy-hemoglobin, melanin and water (see Figure 1.8). The results of skin diffuse reflectance spectra, measured *in vivo* by the experimental setup presented in Figure 1.21, have been used to compare with the results of MC. The resulting images have been textured using a human skin surface BRDF mask (see Fig. 1.23 and Fig. 1.24). Converting the spectral power distribution to the CIE XYZ coordinates and then to the actual RGB-gamut color images is done using the standard observer/tristimulus values utilizing D65 illuminant (Figure 1.22).

The absorption properties of skin tissues in the visible and NIR spectral region were estimated by taking into account the anatomical structure of skin as determined from histology, including the spatial distribution of blood vessels, water and melanin content. Reasonable estimates for oxygen saturation (based on likely metabolic demand) and hematocrit are also included, although these parameters are less well defined than the others as they cannot be determined from post-mortem samples. It has been demonstrated that when a computational model of skin is used with reasonable physical and structural parameters, as described above, the results of skin diffuse reflectance spectra MC simulation are reasonably well-fitted with the results of *in vivo* skin spectra measurements [99].

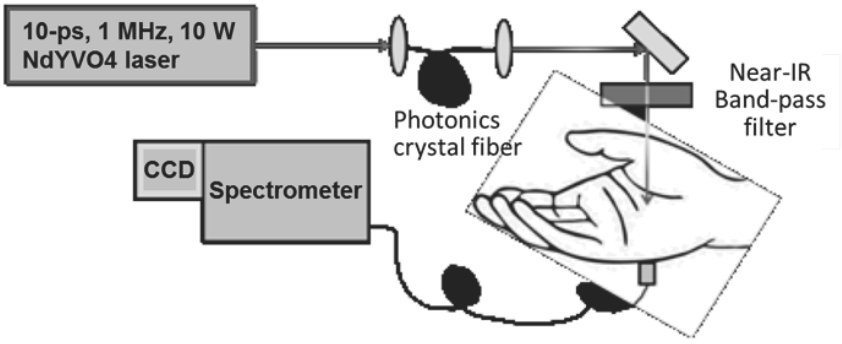

Figure 1.21: Schematic diagram of the experimental set-up. A stable white-light continuum is generated using a large-area photonic crystal fiber and using the near-IR (650-1000 nm) portion of this continuum (roughly, 0.7 W average power) for tissue illumination, while employing a TE-cooled CCD camera (Andor, Inc.) attached to a spectrometer (Horiba, Inc.) for signal detection. An 0.6-mm2-area multimode fiber bundle was used to collect light on the back of the tissue under study. For all the described measurements, the signal was corrected for a background, normalized to the incident light and averaged over 20-s to maximize the signal-to-noise-ratio.

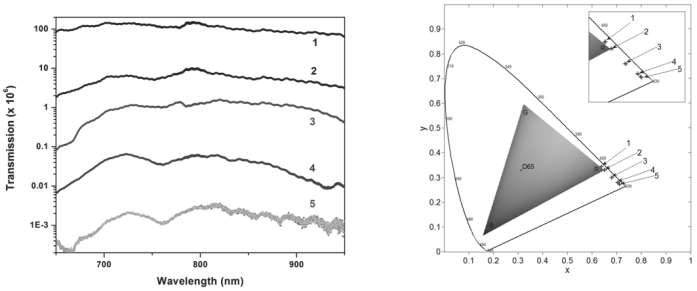

Figure 1.22: The experimental results of transmittance spectra measured for fingernail (1), finger (2), palm (3), wrist (4) and arm (5) *in vivo* (left), and corresponding chromaticity coordinates measured *in vivo* (crosses) and simulated by MC (circles) presented on the CIE 1931 color space (right, represented as gray scale).

The results of the simulation are remarkably similar to the experimentally measured skin spectra in the visible 450-600 nm. The difference in the results of the simulation and the experimental data in the NIR spectral region are explained by the choice of the optical properties of the skin layers, i.e. it was that the scattering properties of all skin layers (i.e. μ_s and g) are wavelength independent.

Thus, based on the transmittance spectra obtained for fingernail, palm, wrist and arm *in vivo*, the chromaticity coordinates are calculated and the regularities of color variation are analyzed by MC simulation. The spectral color composition of biological tissues can be used for express-analysis of their functional physiological condition and identification of the most optimal conditions for diagnostics and treatment.

1.5.3 Sampling volume

Figure 1.25 schematically presents an example of the medium with a fiber optic probe. Due to multiple scattering in the medium, optical radiation is distributed within a certain region G (see

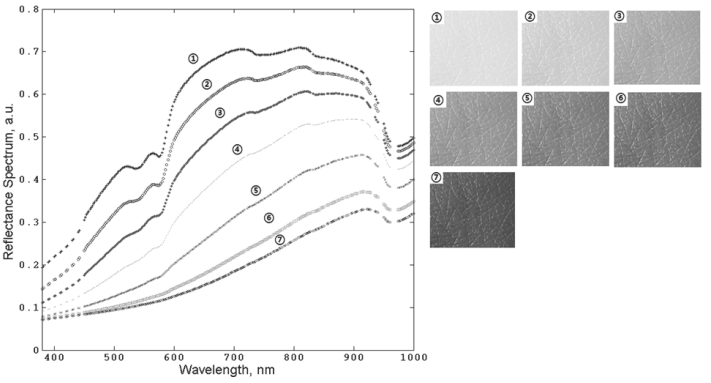

Figure 1.23: The results of MC simulation of human skin spectra (left) and corresponding colors (right, represented as gray scale) while varying the melanin content in Living epidermis.

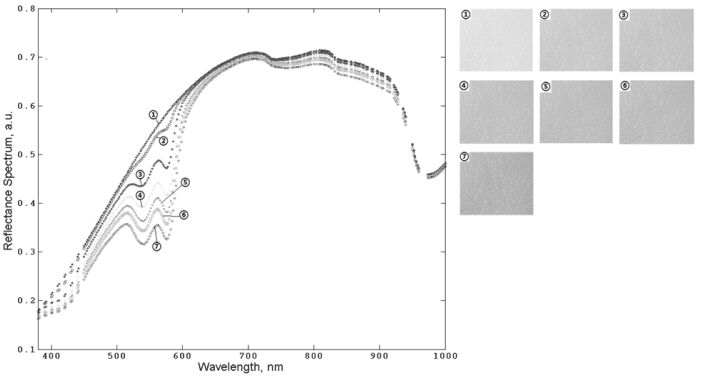

Figure 1.24: The results of MC simulation of human skin spectra (left) and corresponding colors (right, represented as gray scale) while varying the blood concentration in the layers from papillary dermis to subcutaneous tissue.

Fig. 1.25). The region G and the features of the optical radiation distributed within the medium are of predominant interest in dosimetry applications [90].

For OD applications, the spatial distribution of the detected signal (the sampling volume) J is of greater importance. The sampling volume J is formed by the so-called effective optical paths, which are those paths that photons have followed after being emitted at the source and ultimately received by the detector (Fig. 1.25). These photons can traverse many different paths between the source and the detector, some paths being more likely than others. Arridge [198] demonstrated that if represented as a function of a point $\mathbf{r}'$ *in* the medium, the sampling volume $J(\mathbf{r}')$ can be interpreted as the measure (conditional pdf) of the sensitivity of a surface measurement to the interrogated volume of a tissue located at the depth $\mathbf{r}'$. If the region $\delta V(\mathbf{r}')$ attenuates photons at rate α (due to absorption), then the measurement is perturbed, and in the limit $\alpha \to 0$, the rate change of the measurement with the perturbation is given by $J(\mathbf{r_q}, \mathbf{r_m}, \mathbf{r}')$. Note, that only photons that originally passed through $\delta V(\mathbf{r}')$ could have contributed to the change in signal measurement. Hence $J(\mathbf{r_q}, \mathbf{r_m}, \mathbf{r}')$ represents a conditional pdf with the maximum value in the region, which is the most probable origin of the detected signal.

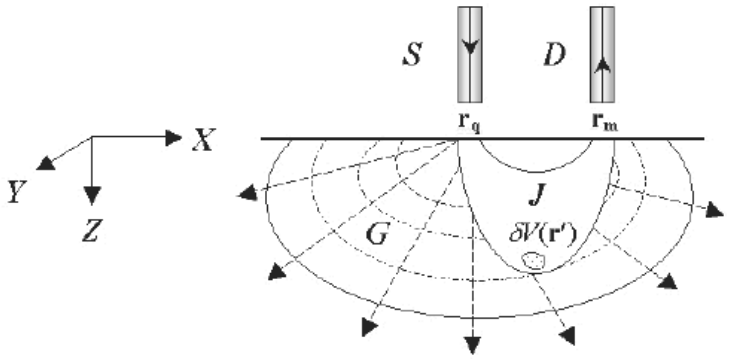

Figure 1.25: Diagram presenting the definition of sampling volume. G is the spatial distribution within semi-infinite scattering medium: J ($J \subset G$) is the spatial distribution of the effective optical paths, passed through a volume $\delta V(\mathbf{r}')$ ($\forall \mathbf{r}' \in J$), source ($S$), detector ($D$).

For experiments involving the backscattered intensity measurements $J(\mathbf{r}')$ is defined as:

$$J(\mathbf{r_q}, \mathbf{r_m}, \mathbf{r}') = \frac{\partial A(\mathbf{r_q}, \mathbf{r_m})}{\partial \mu_a(\mathbf{r}')}, \tag{1.95}$$

where $\partial \mu_a(\mathbf{r}')$ is a perturbation of the absorption coefficient at a point $\mathbf{r}'$. $\partial A(\mathbf{r_q}, \mathbf{r_m})$ is a perturbation of attenuation A at a point $\mathbf{r_m}$ of the detector, while the source of radiation is located at a point $\mathbf{r_q}$ [67, 198, 199]. Attenuation A is defined as

$$A(\mathbf{r_q}, \mathbf{r_m}) = -\ln\left(\frac{I(\mathbf{r_m})}{I_0(\mathbf{r_q})}\right). \tag{1.96}$$

Here, $I_0(\mathbf{r_q})$ is the intensity of incident radiation at a point $\mathbf{r_q}$, $I(\mathbf{r_m})$ is the intensity of the detected backscattered radiation at a point $\mathbf{r_m}$ (see Fig. 1.25). Combining (1.95) and (1.96), $J(\mathbf{r_q}, \mathbf{r_m}, \mathbf{r}')$ takes the form of

$$J(\mathbf{r_q}, \mathbf{r_m}, \mathbf{r}') = -\frac{1}{I(\mathbf{r_m})} \frac{\partial I(\mathbf{r_m})}{\partial \mu_a(\mathbf{r}')}. \tag{1.97}$$

A short form of coordinate dependence of the sampling volume is used further in the text, i.e. $J(\mathbf{r}')$ instead of $J(\mathbf{r_q}, \mathbf{r_m}, \mathbf{r}')$.

Thus, the sampling volume $J(\mathbf{r}')$ is defined as the gradient of the specific radiation flux, which is registered by the detector, with respect to the absorption coefficient $\delta V(\mathbf{r}')$ in the medium at point $\mathbf{r}'$, $\mathbf{r}' \in G$. As a function of $\mathbf{r}'$, $J(\mathbf{r}')$ characterizes the complete spatial distribution of the detected optical radiation in the medium and is determined by the spatial distribution of the effective optical paths. For a heterogeneous medium, which consists of several homogeneous components of different optical properties, e.g. seven optically homogeneous layers of skin, the partial components of the sampling volume $J_k(\mathbf{r}')$ are considered, as:

$$J_k(\mathbf{r}') = -\frac{1}{I(\mathbf{r_m})} \frac{\partial I(\mathbf{r_m})}{\partial \mu_{ak}(\mathbf{r}')}. \tag{1.98}$$

The sampling volume $J_k(\mathbf{r}')$ is equal to $< L(\mathbf{r}') >$, which is the mean "effective path length" of the photons of optical radiation traveling through a small volume $\delta V(\mathbf{r}')$ [67]. This gives a recipe for a practical implementation of numerical calculation of the sampling volume.

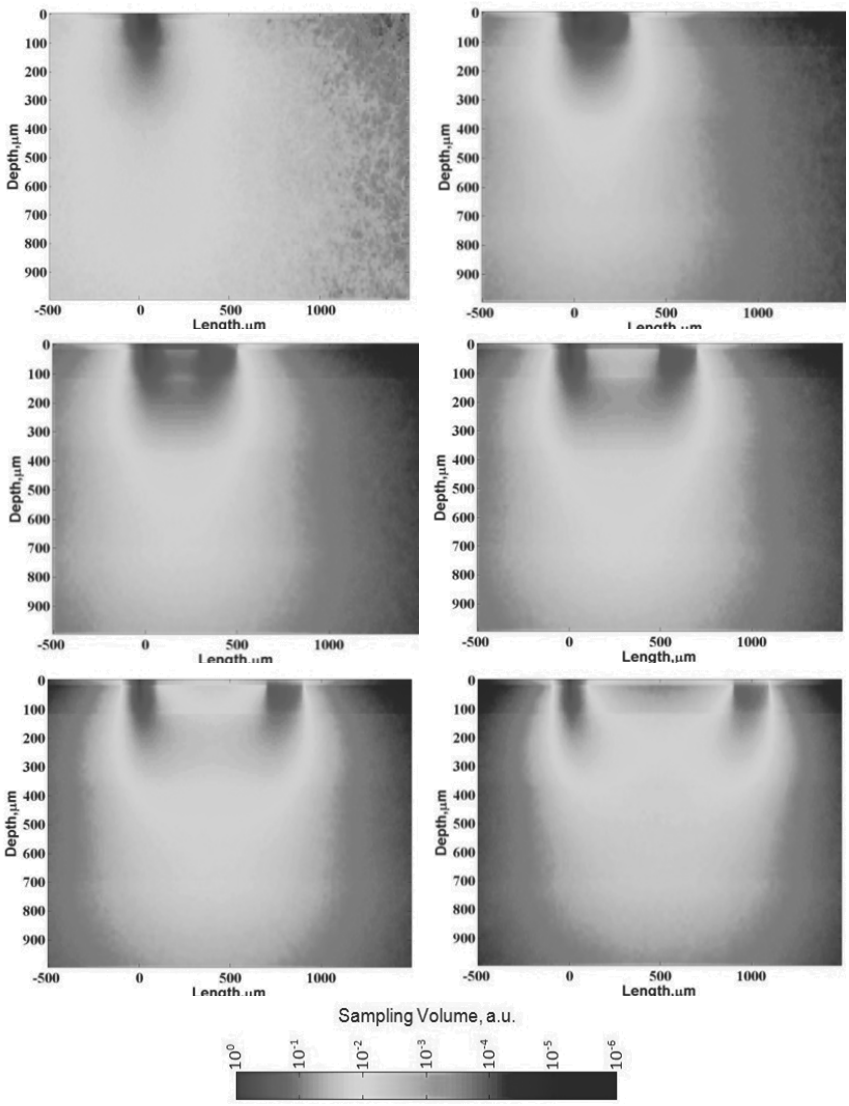

Figure 1.26: (See color insert.) The results of the MC simulation of detector depth sensitivity for a particular optical probe for human skin while varying the separation between source (200 μm) and detector (200 μm): (a) 0.0 μm, (b) 200 μm, (c) 300 μm, (d) 400 μm, (e) 600 μm, (f) 800 μm, (g) 1000 μm, respectively.

MC numerical simulation is the optimal technique for estimation of the pdf of the effective optical paths, i.e. the sampling volume. Once a photon packet is registered by the detector, its trajectory from the source to the detector is weighted by the final statistical weight. Having divided the modeling medium into pixels (e.g. $10\mu m \times 10\mu m \times 10\mu m$) and following the trajectory of each photon

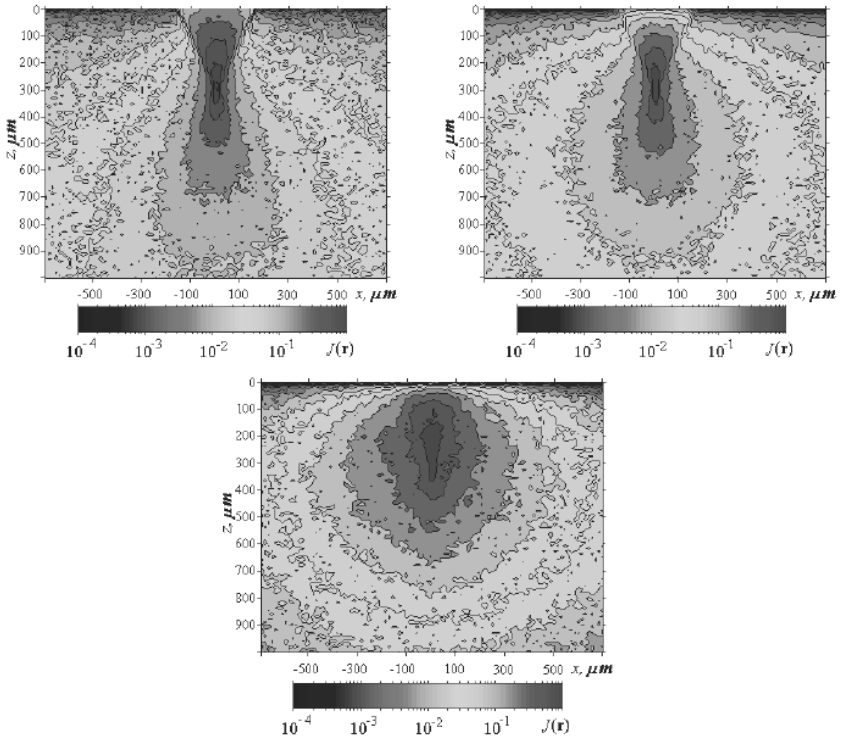

Figure 1.27: Sampling volume $J(x,z)$ for a highly scattering homogeneous medium: (a) $\mu_s = 10$ mm^{-1}; (b) $\mu_s = 26.6\ mm^{-1}$; (c) $\mu_s = 100\ mm^{-1}$. Other optical parameters are $g = 0.9$, $\mu_a = 0.01\ mm^{-1}$, $n = 1.4$. The depth of focal plane $z_f = 300\ \mu$m.

packet from pixel to pixel, the sampling volume $J(\mathbf{r}')$ in a pixel is accumulated as follows:

$$J(\mathbf{r}') = -\frac{1}{I(\mathbf{r_m})}\frac{\partial I(\mathbf{r_m})}{\partial \mu_a(\mathbf{r}')} = \frac{\sum\limits_{i=1}^{N_{ph}} l_i(\mathbf{r}')W_{di}(\mathbf{r_m})}{l_0 \sum\limits_{i=1}^{N_{ph}} W_{di}(\mathbf{r_m})}. \tag{1.99}$$

Here W_{di} is the final weight of the i-th detected photon packet given by (1.46), N_{ph} is the total number of the detected photon packets, $l_i(\mathbf{r}')$ is a path length traversed by the i-th photon packet in a pixel with a center at $\mathbf{r}'$, l_0 is the size of the pixel. Finally, the sampling volume is represented by a 2D cross section map $J(x,z)$, where x is the horizontal axis and z is the depth direction. To determine the path length l_i in a pixel, the algorithm based on the Cohen-Sutherland line clipping method is implemented. The results of the sampling volume modeling for an optical probe for human skin (see the parameters in Table 1.2) are shown in Figure 1.26.

The results of numerical simulation of the sampling volume $J(x,z)$ for confocal probe [200, 201] are presented in Fig. 1.27. The parameters were taken close to those of a typical confocal scheme [202]. Optical parameters of the medium were estimated in accordance with experimental data [203] that defines the maximum penetration depth of confocal probe.

As expected, when the depth of focal plane z_f is less than 3-4 mean photon path lengths l ($\mu_s \leq 10\ mm^{-1}$ or $l \geq 100\ \mu$m), sampling volume $J(x,z)$ reveals a distinct region at the depth of 300 μm, where the majority of the detector photons have been focused. Increasing z_f, the depth of focal plane in the medium, up to about 8-20 mean photon path lengths l ($\mu_s = 26.6$-$40\ mm^{-1}$ or $l =$

25-37.5 μm) does not affect $J(x,z)$ so that the general tendency for photon localization remains unchanged. However, in this case the contrast of the image is expected to reduce because the central focal spot has been enlarged (see Fig. 1.27 b). Increasing the depth of focal plane z_f even further ($\mu_s > 100\ mm^{-1}$ or $l < 1$ μm) will result in a complete refocusing of the incident optical radiation, though it is still well focused.

These results give a perception of how the signal detected during confocal probing localizes in the homogeneous medium. They are also in agreement with the experimental data and the predications of alternative modeling techniques [61, 204, 205].

1.5.4 Fluorescence

Earlier MC schemes of fluorescence modeling consist of the three simulation steps [206, 207, 208, 209]. First, the fluence rate distribution within a tissue volume is calculated by the standard MC scheme [63, 69]. At the second step, spatial fluorescence distribution is obtained by multiplying the fluence rate distribution by the intrinsic fluorescence profile, which is defined as the product of the absorption coefficient of the fluorophore at the excitation wavelength and its quantum yield at the emission wavelength. Finally, the detected fluorescence is calculated as the convolution of the fluorescence source distribution throughout the tissue with the Green's function. In the framework of this model, the intensity of the simulated local fluorescence is proportional to the fraction of the absorbed energy that is determined by the quantum yield of the fluorophore. The fluorescence source distribution within the medium is mainly dependent on the fluence rate distribution. Crille et al. [210] employed the MC fluorescence forward-adjoin model. This MC scheme utilizes the solution of a transport equation both in forward (excitation photon) and in adjoin (fluorescent photon) calculations. The solution of the adjoin transport equation is obtained for those fluorescence photons that contribute to the detected fluorescence signal.

Another scheme of an independent simulation of the fluorescence acts has been proposed [211]. In this approach, the emission of the fluorescence photons occurs at the scattering sites and the quantum yield of a fluorophore γ serves as the fluorescence threshold probability (Figure 1.28 a). The intensity of simulated fluorescence is defined by the fraction of the absorbed radiation $W_{i-1} - W_i$ (see Fig. 1.28 a). In a more plausible model of fluorescence simulation [212, 213], the fluorophore absorption μ_{af} is separated from the total medium/layer absorption by the standard rejection scheme based on the fluorophore absorption threshold $P_a = (1 - \exp(-\mu_{af} l_i))$ (Fig. 1.28 b). Here, the intensity of generated fluorescence is equal to the product of the quantum yield and the intensity of the incident radiation, γW_{i-1}. In this model, each photon packet produces only one fluorescence photon. Both models have assumed that the fluorescence is emitted uniformly from the scattering sites in random directions (see Fig. 1.28 a, b).

A possibility to incorporate in MC spatial distribution of fluorescence has been suggested in [166, 214]. The fluorescence excitation is determined as:

$$W_{em}(\mathbf{r}) = W(\mathbf{r}) P_a P_\rho P_\gamma, \tag{1.100}$$

where $W(\mathbf{r})$ is the photon weight at a point $\mathbf{r}$ and is equal to the probability that the photon packet has reached a point $\mathbf{r} = \mathbf{r}(x,y,z)$ in the medium; P_a is the probability of the photon packet absorption at the i-th step; P_ρ is the probability of absorption by the fluorophore non-uniformly distributed within the medium; P_γ is the probability of the fluorescence excitation determined by the fluorophore quantum yield γ. The probabilities P_a, P_ρ, P_γ are calculated by the standard rejection scheme [72]. In contrast to the models [206–213] (Fig. 1.28 a and b), where fluorescence is emitted between scattering events, following spatial distribution of fluorophores in tissues (Figure 1.29), e.g. collagen distribution for autofluorescence [166, 214].

spatial distribution of the fluorophores is described as $\cos(k\rho)\cos(kz)$, where $k = \pi/d$; d is the collagen fiber diameter; $\rho = \rho(x,y)$ and z are the coordinates of a point in the medium. The non-homogeneous distribution of fluorescence within the dermal layers is clearly illustrated in the ex-

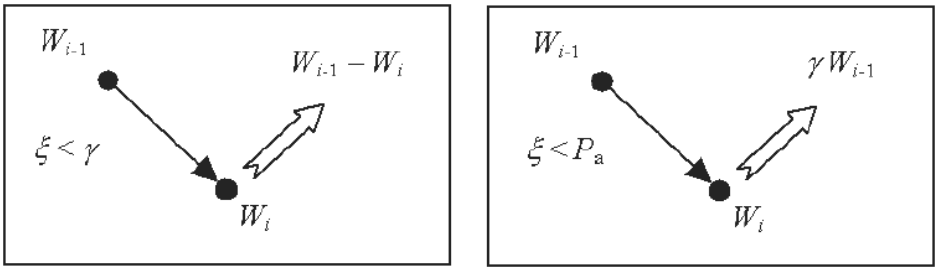

(a) (b)

Figure 1.28: Schematic representation of the MC fluorescence simulation: (a) the fluorescence probability is determined by quantum yield γ of a fluorophore [211]; (b) each fluorescence event is determined by the probability of the photon packet absorption $P_a = (1 - \exp(-\mu_{af} l_i))$ [212, 213]. W_{i-1} and W_i are the statistical photon weights at the $(i-1)$-th and i-th steps of the photon packet; μ_{af} is the fluorophore absorption coefficient; l_i is the path length of a photon between the scattering events; $\xi\,(0 \le \xi \le 1)$ is the uniformly distributed random number used in the rejection scheme.

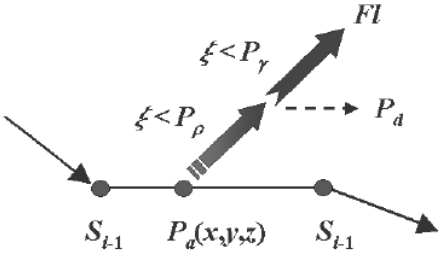

Figure 1.29: Schematic representation of the fluorescence modeling: P_a is probability of the photon packet absorption between two scattering sites S_{i-1} and S_i; P_r is the probability of the absorption by the fluorophore; P_γ is the probability of the fluorophore fluorescence determined by the fluorophore quantum yield γ; $P_d = (1 - P_\gamma)$ is the probability of dissipation determining a fraction of absorbed energy exerted non-radiative relaxation through other mechanisms, e.g. thermal excitation or phosphorescence, etc.; $\rho(x,y,z)$ determines spatial fluorophore distribution within the medium.

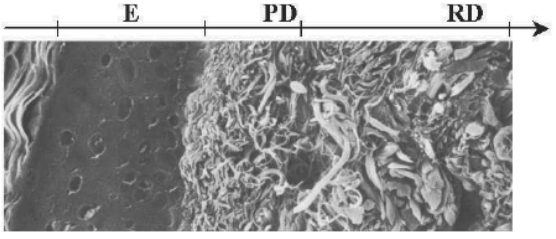

Figure 1.30: The scanning electron micrograph taken from [215] shows the arrangement of collagen fibers in the dermis (with permission). Fiber bundle diameters and density of packing in the papillary dermis (PD) and reticular dermis (RD) are different. Collagen is organized in long, wavy bundles, which vary in diameter from about 1-40 μm. Collagen bundles interweave in a complex and random manner to form a three-dimensional irregular meshwork [107, 216].

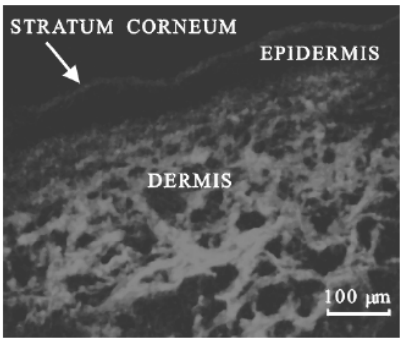

Figure 1.31: Experimental autofluorescence image of skin tissue section under illumination of 442 nm laser radiation. (Courtesy of Dr. H. Zeng, from [208]. With permission).

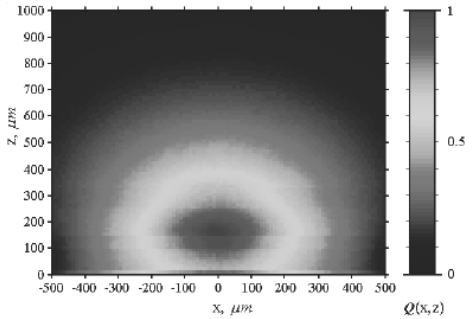

Figure 1.32: Two-dimensional distributions of the spatial depth sensitivity $Q(x,z)$. The optical parameters of skin layers were chosen for 488 nm. The fractions of fluorescence that are sensitive to sensor and topical dermal layers are close. The diameter and numerical aperture of detector are equal to $D = 1000$ μm and $NA = 0.63$; acceptance angle $\theta_d = \sin^{-1}(NA/n_0) = 40^0$.

perimental images of autofluorescence of human skin (Figure 1.31), whereas the distribution of fluorophores in the stratum corneum and the epidermis seems to be homogeneous [208].

The fluorescence photons are emitted isotropically from the source points, which agrees with the assumptions proposed in earlier works [206–213].

The spatial distribution of fluorescence excitation is accumulated as a set of coordinates (x,y,z) and photon weights W_{em}. The fluorescence photons are emitted until the necessary number of photon packets collected by a detector is achieved. The MC method is employed to propagate fluorescence photons, however, new values of the optical parameters corresponding to emission wavelength are used.

To express the sensitivity of a surface measurement (a detection system) to interrogated volume of the tissue the detector depth sensitivity (the sampling volume) is employed. Here, the sampling volume $Q(\mathbf{r})$ is defined as the gradient of fluorescent radiation density with respect to the absorption coefficient of a small region of medium at the point $\mathbf{r}$.

The described MC model has been applied to assess spatial distribution of both skin tissue autofluorescence and fluorescence excitation of the smart "tattoo" sensor layer. Optical parameters of skin tissues used in the simulation are shown in [166, 214].

Additional MC simulation was carried out to illustrate how the localization of fluorescence excitation and the sampling volume are affected by excitation at longer wavelength. For this case the

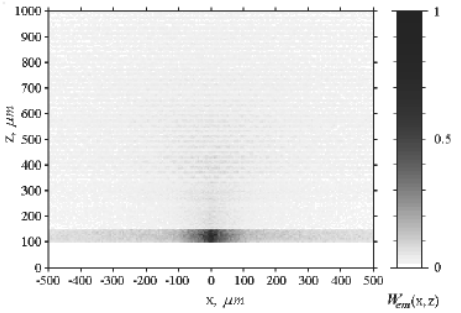

Figure 1.33: Spatial distribution $W_{em}(x,z)$ of the fluorescence excitation of the "tattoo" sensor layer and autofluorescence excitation in human skin in the near infrared spectral region. Excitation of autofluorescence in the dermal layers is highly ($\sim$ 4-5 times) suppressed due to the low fluorescence efficiency of natural fluorophores in the near infrared spectral region. The main fluorescence excitation is localized in the sensor layer. The modeled skin tissue's optical properties were chosen for 700 nm. The diameter of source is equal to 200 μm. The incident beam has a uniform geometry profile.

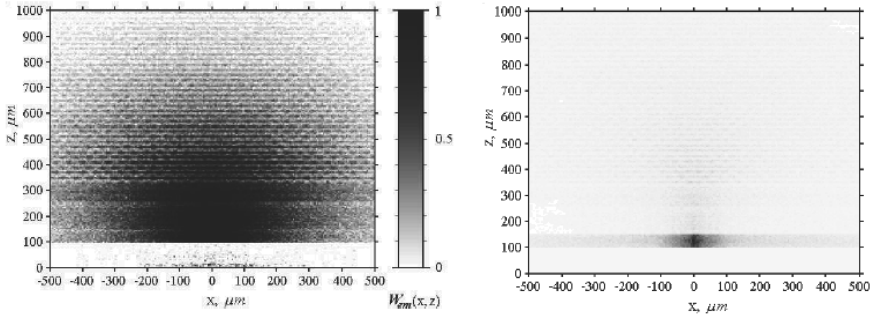

Figure 1.34: Spatial distribution of the fluorescence excitation for the refractive index matching ($n = 1.5$): (a) - visible spectral region 488 nm; (b) - near infrared spectral region 700 nm.

modeled skin tissue's optical properties were chosen for 700 nm. Due to the monotonically decreasing scattering of skin tissue with wavelength in the range 450-1100 nm [68, 114] the scattering coefficients μ_s are reduced by a factor of 2–3, whereas the absorption coefficients of the skin layers are taken to be a factor of ten less [90]. Scattering of the sensor layer was believed to be close to that of the epidermis, while its absorption coefficient was taken unchanged, that presumed the usage of the near infrared fluorophore [217]. The low fluorescence efficiency of endogenous fluorophores in the near infrared spectral region [218] was simulated by their reduced absorption; quantum yields of biotissues were kept unchanged.

The results of the simulation are presented in Figure 1.33. The results show that excitation of autofluorescence in the dermal layers is highly ($\sim$ 4-5 times) suppressed due to the low fluorescence efficiency of natural fluorophores in the near infrared spectral region [218] and the main fluorescence excitation is localized in the sensor layer. Nevertheless, the periodic structure of fluorescence excitation in the dermal layers is still observed.

The MC technique has been applied for modeling the fluorescence excitation and assessing of

the sampling volume within the skin. The simulation results show that the maximum of the fluorescence excitation sources is localized in the topical dermal and in the "smart" sensor ("tattoo") layers. Spatial distribution of the fluorescence excitation within dermal layers demonstrates a good correlation to experimental autofluorescence image of skin tissue. When moving to the near infrared spectral region, the fraction of the autofluorescence excitation is significantly reduced and the sampled area is predominately localized in the "tattoo" sensor layer. Refractive index matching at skin interface produces a remarkable enhancement of the sampling volume localization. The maximum of the detector depth sensitivity is shifted to the "tattoo" sensor layer and moves away from the stratum corneum and the epidermis. The simulations have revealed a general tendency of optical/fluorescence measurements to localism in a small shallow volume in the "tattoo" sensor layer. It is concluded that the results of this study accompanied by recent progress in biophotonics can be beneficial to a number of applications aimed towards medical diagnostics and general physiological studies.

1.5.5 Coherent effects and polarization

The MC method has been extensively used to simulate the coherent effects of multiple scattering including temporal field correlation function, the CBS intensity and the helicity flip of circularly polarized light [135, 137, 168, 169, 219–224]. For a semi-infinite isotropic, scattering, and non-absorbing medium, the intensity of single and double scattered photons can be estimated analytically:

$$\begin{aligned} I_{single} &= l^{-1}\int dz_1 \int d\mathbf{R}_2 \delta(\mathbf{R}_2-\mathbf{R}_1)\exp(-\frac{2z_1}{l}) = 1/2, \\ I_{double} &= (4\pi)^{-1} l^{-2}\int dz_1 \int d\mathbf{R}_2 \Lambda_0(\mathbf{R}_2-\mathbf{R}_1)\exp(-\frac{z_1+z_2}{l}) = \ln\sqrt{2}, \end{aligned} \tag{1.101}$$

where z_1 and z_2 are the distance from the scattering points. For isotropic scattering the phase function $p_0(\mathbf{k}_i-\mathbf{k}_s) = \frac{1}{4\pi}$. Moreover, for isotropic scattering an exact Milne solution is available that, for example, gives the ratio of the diffuse reflectance and intensity of the single scattered photons $I/I_{single} = 8.455$ [20]. Several MC simulations have been carried out to define the cut-off criterion, i.e. the minimal weight, maximum number of scattering events, etc. Accuracy of not less than 4 significant digits has been achieved for $N_{ph} = 10^5$, $N_{max\ scat} = 5000$, and $W_{min} = 10^{-3}$.

The results of calculation of the temporal field correlation functions for scattering media with different anisotropy factors $g = 0, 0.5$ and 0.9 are presented in Figure 1.35. The optical properties of a medium are: $\mu_s = 30\ \mathrm{mm}^{-1}$, $\mu_a = 0$, $n = 1$. Thus, the transport of mean free path lengths (MFPs) are $l^* = l/(1-g) = 33.3\ \mu m$, 66.6 μm and 333.3 μm for isotropic $g = 0$, intermediate $= 0.5$ and highly anisotropic $g = 0.9$ scattering media. A semi-infinite medium and a slab of thickness $L = l^*$ are considered.

The obtained results (Fig. 1.35) are reasonably well described by the analytical formula derived from the diffusion approximation [133, 148]:

$$g_1(\tau) \propto \frac{\sinh(\alpha[L+\eta_1-\eta_0])}{\sinh(\alpha[L+2\eta_1])}, \tag{1.102}$$

where $\alpha = (3t/(\tau l^{*2}))^{1/2}$, $\eta_0 = l^*$ is the depth at which the incident light is completely diffused, $\eta_1 \approx (2/3)l^*$ is the extrapolated boundary length. Since the influence of the factor of anisotropy g decreases as a slab becomes thicker, there is a tendency for a better agreement between the results of the MC simulation and predictions of the diffusion theory (Fig. 1.35). This was ascribed to the diminishing role of lower order scattering events, which cannot be properly accounted for within the diffusion theory. Nevertheless, the general tendency of independence on the anisotropy factor g is as obvious for a semi-infinite medium as for a slab. Deviation from the expected linear decay at

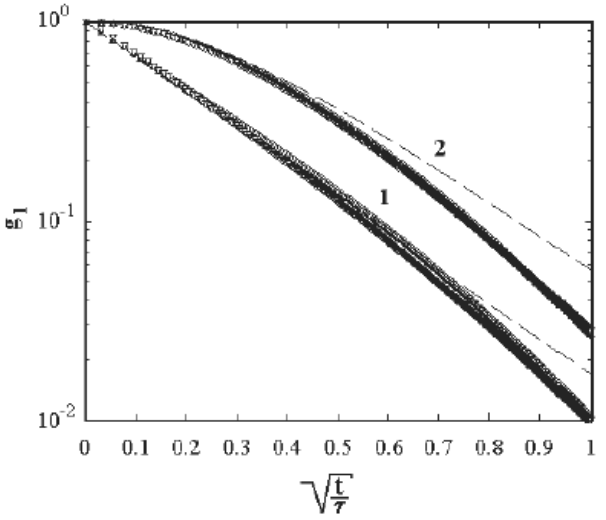

Figure 1.35: The normalized temporal field correlation functions $g_1(t)$ for backscattering radiation versus $(t/\tau)^{1/2}$: semi-infinite medium (1), a slab of thickness $L = l/(1-g)$ (2). Different factors of anisotropy are considered (□) – isotropic $g = 0$, (•) – intermediate $g = 0.5$, and (△) – high anisotropic $g = 0.9$. Dashed lines are approximation (1.102) for a semi-infinite medium and a slab. The optical properties of a medium are: $\mu_s = 30\ \text{mm}^{-1}$, $\mu_a = 0$, $n = 1$.

some time is attributed to the effect of limited number of longer photon paths, which is a result of finite computation time. In time, the contribution of longer paths diminishes, and the requirement of a large number of long-path photons becomes less strict.

The CBS intensity peak is simulated for the same isotropic, intermediate and high anisotropy semi-infinite scattering media. The results of the MC simulation for isotropic scattering show that $h^{CBS} = 1.87$, that agrees very well with the results derived from the generalized solution of the Milne problem: $h^{CBS} = 1.88$ [20]. In limit of $g \to 1$ the theory predicts $h^{CBS} \to 2$, that corresponds with the results of the MC simulation $h^{CBS} = 1.99$ for $g = 0.9$.

Expressed in terms of the dimensionless parameter $\tilde{q} = kl^* \sin\theta_s$, the simulated angular dependence of the CBS exposes typical behavior, indicating that it is practically independent of anisotropy (Fig. 1.36). The results of simulation are compared against the results predicted by the analytical approach [225]:

$$I_{CBS}^{(1)} = \exp(-\gamma kl^* \sin\theta_s) \tag{1.103}$$

or in its linear approximation:

$$I_{CBS}^{(2)} = 1 - \gamma kl^* \sin\theta_s, \tag{1.104}$$

where $\gamma \approx 2$ is the relative slope of the CBS decay (Fig. 1.36). The results of simulation also indicate a universal decreasing trend, whereas the diffusion approximation predicts that the CBS peak falls down with different slope values for different values of the anisotropy factor. Notice that this dependence strongly disagrees with the predictions of the diffusion approximation [138]:

$$I_{CBS}^{(diff)} \propto 1 - 2\frac{(1+z^*)^2}{1+2z^*} kl^* \sin\theta_s, \tag{1.105}$$

which yields the slope $\gamma^{(diff)} \approx 2.3$ for $g = 0$ and $\gamma^{(diff)} \approx 0.71$ for $g \to 1$, where $z^* = 0.71(1-g)^{-1}$ is the Milne extrapolation parameter [226]. To some extent, the results obtained also demonstrate